공학박사학위논문

Tyrosine Peptide Template-based Palladium Nanoparticle Catalyst for C-C Coupling Reaction and Dityrosine Crosslinked Perylene Diimide for Photocurrent Generation

타이로신-펩타이드 주형의 팔라듐 나노입자 촉매를
이용한 탄소-탄소 짝지음 반응 및
다이타이로신으로 가교된 퍼릴렌 다이이미드의
광전류 생성에 대한 연구

2017년 7월

서울대학교 대학원
화학생물공학부
김 영 오

Tyrosine Peptide Template-based Palladium Nanoparticle Catalyst for C-C Coupling Reaction and Dityrosine Crosslinked Perylene Diimide for Photocurrent Generation

타이로신-펩타이드 주형의 팔라듐 나노입자 촉매를 이용한 탄소-탄소 짝지음 반응 및 다이타이로신으로 가교된 퍼릴렌 다이이미드의 광전류 생성에 대한 연구

지도 교수 이 윤 식

이 논문을 공학박사학위논문으로 제출함
2017년 7월
서울대학교 대학원
화학생물공학부
김 영 오

김영오의 공학박사학위논문을 인준함
2017년 7월

위 원 장 김 병 기 (인)

부위원장 이 윤 식 (인)

위 원 김 정 원 (인)

위 원 남 기 태 (인)

위 원 김 대 형 (인)

ABSTRACT

Tyrosine Peptide Template-based Palladium Nanoparticle Catalyst for C-C Coupling Reaction and Dityrosine Crosslinked Perylene Diimide for Photocurrent Generation

Young-O Kim

School of Chemical and Biological Engineering

The Graduate School

Seoul National University

Proteins and peptides systematically assemble into functional systems by using multiple covalent and non-covalent interactions of 20 amino acids. Among various amino acids, tyrosine has unique properties in helping protein folding and facilitating proton-coupled electron transfer. Recently, many efforts have been conducted to apply the tyrosine's properties in fabrication of functional material.

In chapter 1, a fabrication method of palladium (Pd) nanostructure using a specifically designed peptide, Tyr-Tyr-Ala-His-Ala-Tyr-Tyr (YYAHAYY), as a template is described. The YYAHAYY peptide

induced the formation of flower-like palladium (Pd) nanostructure by controlling its size and shape. The flower-shaped Pd NPs were well-dispersed in water due to the amphiphilic property of YYAHAYY peptide. In addition, the flower-shaped Pd NPs showed excellent catalytic activities in copper-free Sonogashira cross-coupling reaction in water.

In chapter 2, a method to self-organize perylene diimides (PDI) into two-dimensional (2D) film at air/water interface through dityrosine crosslinkage is presented. Dityrosine-crosslinking was formed by one-step photo-polymerization of tyrosine-appended PDI without the need of a template. Such assembly is driven by the amphiphilicity of the crosslinked molecules that have the carboxylic group from the tyrosines and the polycyclic aromatic hydrocarbons from the PDIs. Depending on UV irradiation time, the thickness of the film can be controlled. In addition, upon crosslinking, the PDI film is stacked through pi-pi interaction between the PDIs, which induces semi-crystalline property. The resulting dityrosine crosslinked PDI film shows a photo-active property. This simple approach can be expanded into direct fabrication of free-standing and photocurrent generating organic thin films.

Keywords: Peptide assembly, Self-assembly, Bio-inspired approach, Peptide template, Tyrosine, Dityrosine, Palladium, Catalyst, Cross coupling, Copper-free Sonogashira reaction, Organic semiconductor, Perylene diimide,

Photocurrent

Student number: 2011-21021

TABLE OF CONTENTS

LIST OF TABLES

LIST OF FIGURES

LIST OF ABBREVIATIONS

AFM	Atomic force microscopy
ATR	Attenuated total reflection
CAPS	*N*-Cyclohexyl-3-aminopropanesulfonic acid
CD	Circular dichroism
CTC	2-chlorotrityl chloride
DIPEA	N,N-diisopropylethylamine
DODT	3,6-dioxa-1,8-octanedithiol
EDS	Energy-dispersive X-ray spectroscopy
fnIII	Fibronectin type III
FT-IR	Fourier transform infrared spectroscopy
GC-MS	Gas chromatography-mass spectrometry
Gly	Glycine
HBTU	2-(1*H*-benzotriazole-1-yl)-1,1,3,3-tetramethyluronium hexafluorophosphate
HCl	Hydrochloric acid
His	Histidine
HOBt	Hydroxybenzotriazole
HR-TEM	High resolution transmission electron microscopy
ICP-AES	Inductively coupled plasma-atomic emission spectroscopy
IDE	Interdigitized electrode
Ig	Immunoglobulin
Na_2PdCl_4	Sodium tetrachloropalladate
NF	Nanoflower
NMR	Nuclear magnetic resonance
NP	Nanoparticle
PA	Peptide amphiphile
PCET	Proton-coupled electron transfer
PDI	Perylene diimide
PSAM	Peptide self-assembly mimic

PS II	Photosystem II
PTCDA	Perylene tetracarboxylic acid dianhydride
RGD	Arg-Gly-Asp
RNR	Ribonucleotide
ROESY	Rotating-frame nuclear Overhauser effect correlation spectroscopy
TA	Transient absorption
TEA	Triethylamine
TEM	Transmission electron microscopy
TIPS	Triisopropylsilane
Tyr	Tyrosine
Tyr-A7mer	Tyr-Tyr-Ala-Ala-Ala-Tyr-Tyr
Tyr-H7mer	Tyr-Tyr-Ala-His-Ala-Tyr-Tyr
XRD	X-ray diffraction
Y-PDI	Tyrosine-appended perylene diimide
YG-PDI	Tyr-Gly-appended perylene diimide

Tyrosine Peptide Template-based Palladium Nanoparticle Catalyst for C-C Coupling Reaction and Dityrosine Crosslinked Perylene Diimide for Photocurrent Generation

Introduction

1. Peptide Assembly Based Architectures

Self-assembly is a powerful tool for making organized, ordered supramolecular architectures at nano- or macroscopic scales. This "Bottom-up" approach is generally induced via non-covalent interactions such as hydrophobic interaction[1-3], hydrogen bonding[4,5], electrostatic interaction[6,7], metal-ligand coordination[8] and pi-pi stacking[9,10]. Such molecular recognition-directed self-organization is determined by the intrinsic features of a molecular structure, which determine the thermodynamic factors[11], resulting in functional materials with particularly designed features. In addition, kinetic controlling parameters such as solvent[12,13], temperature[14], and concentration[15] can be used to manipulate self-assembly process. Eventually, the self-assembly processes are driven by the complex harmony of thermodynamic and kinetic factors (Fig. 1).

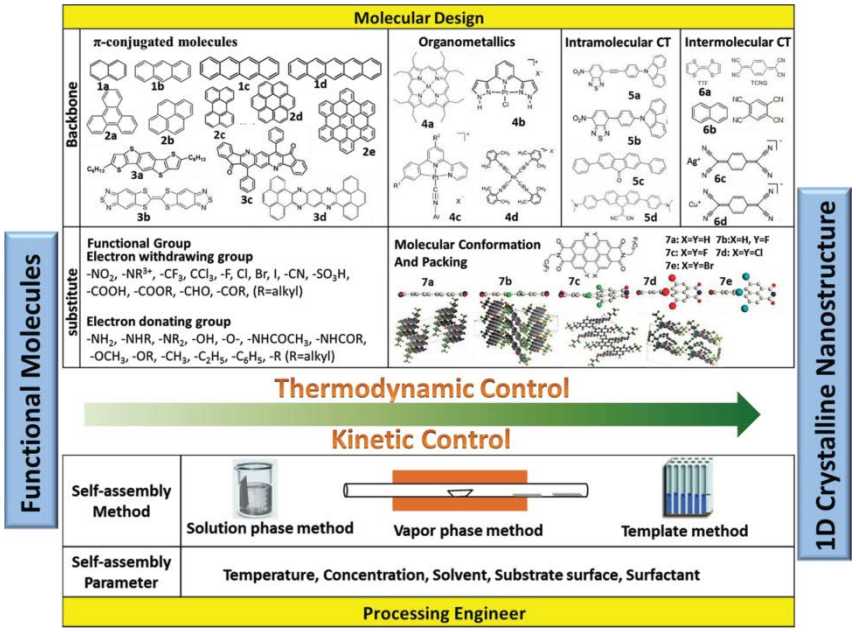

Figure 1. Summary of thermodynamic and kinetic control factors for engineering nanostructures.[11]

Due to a surge of interest in using bio-derived materials, self-assembly of proteins or peptides into nanostructures receives a great deal of attention in a range of potential applications in biomedicine, material science and nanotechnology (Fig. 2A).[16-22] The peptide materials have the advantage of diversifying physicochemical properties by tuning peptide sequences consisting of 20 amino acids. In the early stage, Ghadiri group suggested at methodology for producing peptide-based nanotubes, so that the amide bonds of a cyclic octapeptide, *cyclo*[-D-Ala-Glu-D-Ala-Gln]$_2$, can induce a nanotubular packing (Fig. 2B).[23] In addition, Gazit group unearthed the very short peptide, diphenylalanine (Phe-Phe), from amyloid plaques formed by mis-folding of normal protein in Alzheimer's disease patients (Fig. 2C).[24] Following these, a variety of peptide sequences[25-30], which are part of various protein fragments associated with biological functions, and diphenylalanine derivatives[31-34] have been investigated, and variegated morphologies such as tubes[35-37], spheres[38-40], planes[41-44] and 3D networks[45-47] have been reported.

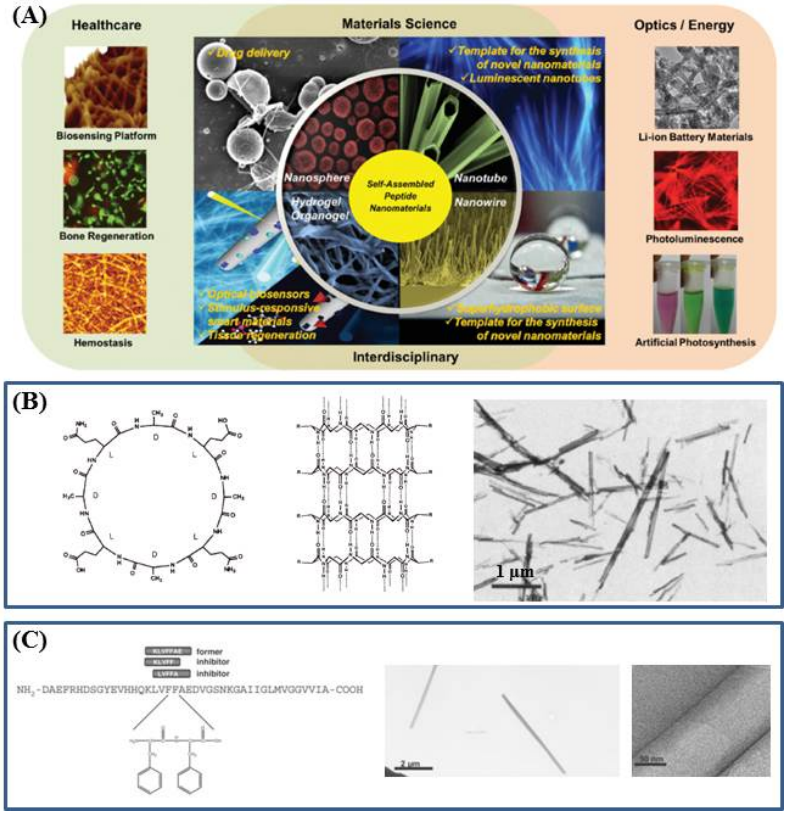

Figure 2. (A) Peptide-based nanostructures applicable to various research fields.[48] (B) Nanofiber formed by hydrogen bonding from designed cyclic peptide.[23] (C) Short peptide sequence (Phe-Phe) derived from amyloid plaques in Alzheimer's disease patients and its self-assembled structure.[24]

For predictable design of nanostructures having functionality, Stupp group systematically designed and synthesized nanofiber forming peptide amphiphiles (PAs), which are surfactant-like structure composed of a hydrophobic long alkyl tail, a short peptide sequence inducing intermolecular hydrogen bonding, a solubility controlling sequence containing charged amino acids, and functional sequences expressed on the surface (Fig. 3).[22,49,50] First, the hydrophobic tails have 12-16 carbon atoms in length, which are segregated away from water and drive assembly.[51] Second, the hydrogen bonding domain play an important role in directing the self-organization into fibric structure by changing the secondary structure.[52] Third, the charge-carrying domain determines not only the initiation of the self-assembly condition (pH, ion, and so on) but also the balance between the electrostatic repulsion and the assembly propensity.[22,53,54] Finally, the last domain has little effect on the geometrical factor. Thus, the specific peptide sequences, such as the Arg-Gly-Asp (RGD) that has a role of integrin-mediated cell adhesion[55-57], can be incorporated to this region for various purpose.

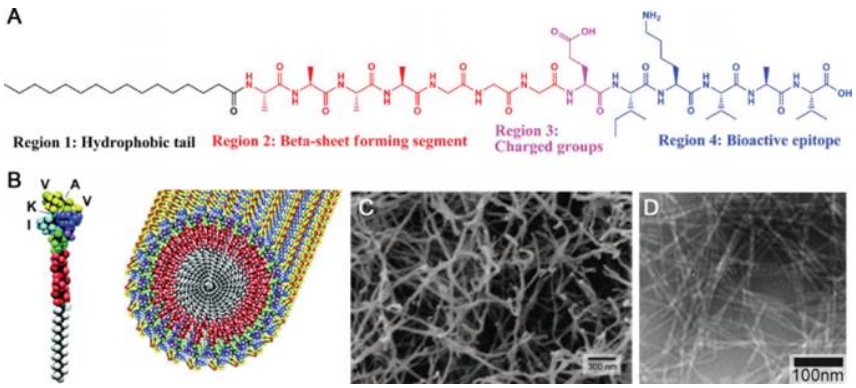

Figure 3. Structure and self-assembly of peptide amphiphile (PA). (A) Representative PA structure with rationally designed functional entities.[22] (B) Illustration of PA nanofiber expressing IKVAV bioactive epitope on its surface.[50] (C) SEM image of self-assembled PA structure. (D) TEM image of self-assembled PA structure.

Recently, based on the previous experimental information about peptide-related structures, short peptide sequences have been systematically designed.[58-60] Particularly, Ulijn group discovered tri-peptide sequences for assembling into nanostructures under aqueous and neutral conditions using computational tools (Fig. 4).[61] However, no common methods exist to predict specific peptide sequences that can have desired functions and structures.

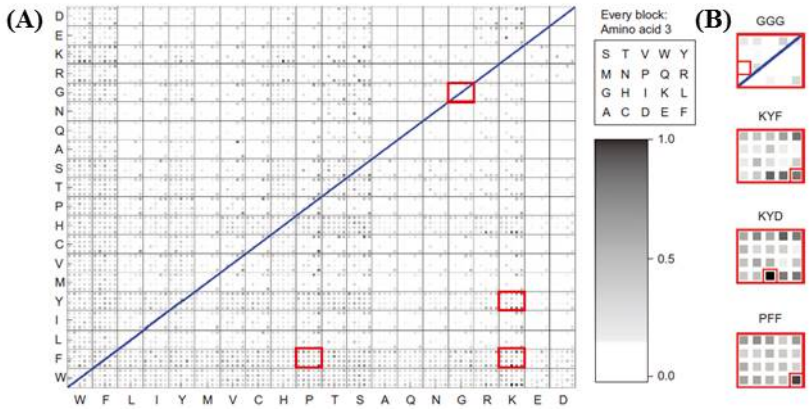

Figure 4. Assembling propensity table of all 8,000 combinations of three amino acids. The darkness of the squares in every rectangle represents the third amino acid-dependent aggregation level.[61]

2. Properties of Tyrosine

Among 20 amino acids, tyrosine (Tyr) is a versatile amino acid that regulates the conformational transition of peptides or proteins, and has redox active property in natural system.

2.1. Tyrosine as a Structure Forming Inducer

Being different form phenylalanine, tyrosine moiety has a phenolic -OH group as a side chain functional group (Fig. 5).[62] In addition, it has a character of beta-sheet forming propensity[63,64] and affects the fibril lamination[65]. In this context, various proteins such as Greek key beta-barrel protein, immunoglobulin (Ig), and fibronectin type III (fnIII) have the tyrosine-containing local motif, so called “tyrosine corner”, where the phenol group of tyrosine forms a hydrogen bond with nearby peptide backbone [CO or NH], forming a folding nucleus and its stabilization (Fig. 6B).[66-69] Moreover, tyrosine cross-strand ladder influences the conformation and the rigidity of a multi-layer stacking in beta-sheet forming protein through the pi-pi interaction between the

aromatic side chains (Fig. 6A).[65]

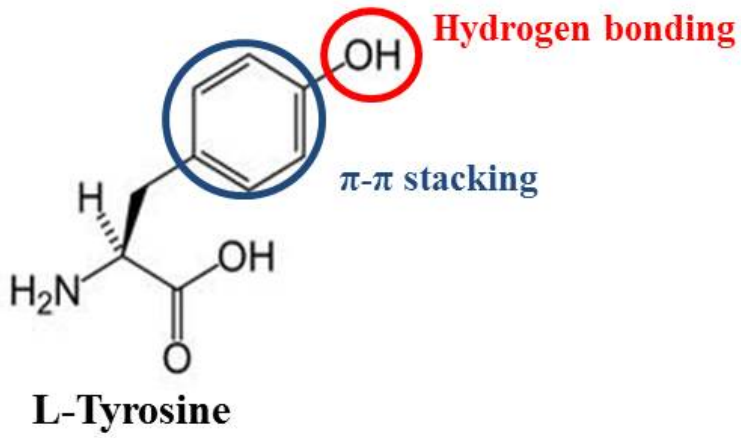

Figure 5. Molecular structure of tyrosine inducing conformational folding with hydrogen bonding and pi-pi stacking.

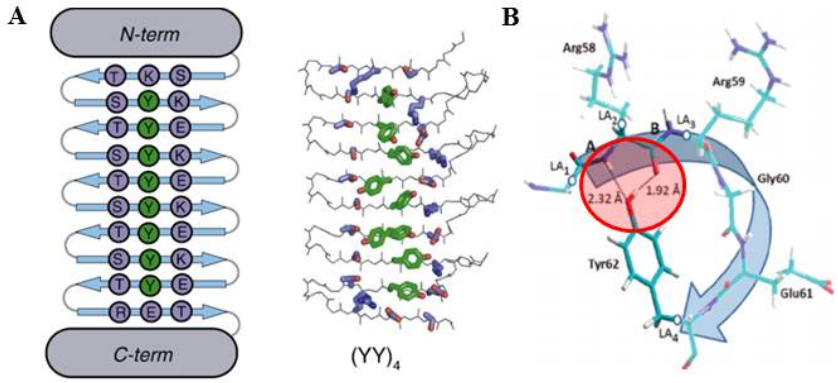

Figure 6. Examples of conformation formed by tyrosine in protein. (A) β-sheet conformation induced by tyrosine ladder at a large scaffold peptide self-assembly mimic (PSAM)[65], and (B) folding by tyrosine corner in human gamma-B-crystallin.[70]

2.2 Tyrosine as Redox Mediator

Charge transfer is an important process for all living organisms. Nature integrates multiple components sophisticatedly for an efficient charge transfer over a long distance. In various biological system such as photosystem II[70], ribonucleotide reductase (RNR)[71] and pilin filament[72-74], pertinent localization of charged and aromatic side chains helps each components to function properly (Fig. 7A-C). In photosystem II (PS II), tyrosine (Tyr) facilitates proton-coupled electron transfer (PCET) controls both the electron and the proton flow (Fig. 7D) and plays an essential role as a mediator or a cofactor of electron traveling by connecting an energy gap between P680 and $CaMn_4$ cluster. Inspired from the role of the tyrosine in enzymatic system and photosynthesis, numerous model studies have been conducted using the structurally defined biomimetic peptide[75-77], such as a beta-hairpin Tyr-containing peptide designed de novo, and Tyr-conjugated metal-ligand complex[78-80] (Fig. 8).

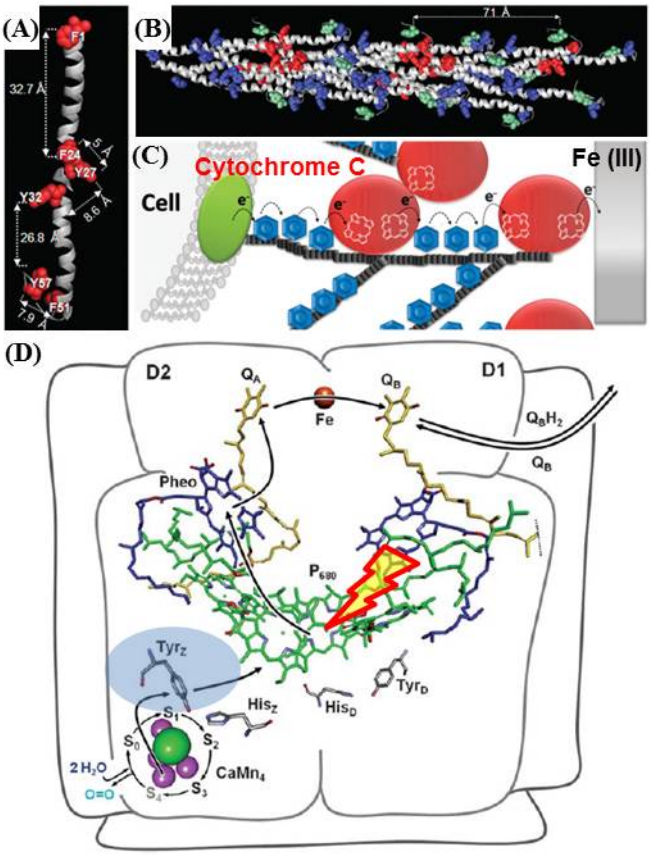

Figure 7. Charge transfer of tyrosine. (A-C) Arrangement of aromatic side chain (tyrosine & phenylalanine) and electron transport mechanism in *Geobacter Sulfurresducens* pili.[74] (D) Tyr-mediated electron flow in photosystem II.[70]

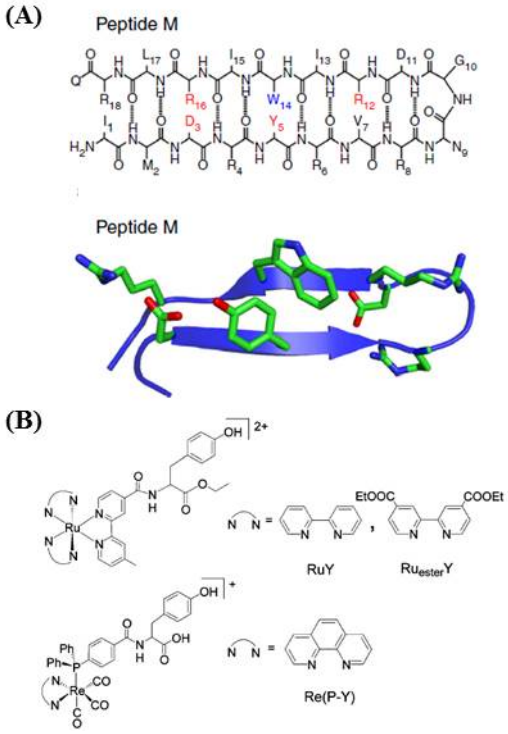

Figure 8. Models for demonstrating proton-coupled electron transfer of tyrosine. (A) A β-hairpin peptide designed for making the environment of redox active tyrosine.[76] (B) Tyrosine-conjugated light absorbing metal-ligand dye for mimicking the photosystem.[79]

2.3. Di-tyrosine as a Crosslinker

Tyrosine has excellent properties not only as a monomer, but also as a tyrosine-tyrosine crosslinking ability, which can be readily accomplished by radiolysis[81], photolysis at 275-280 nm[82-84], metal ions[84-87], enzyme[84] or Ru(II)$(bpy)_3$ dye-mediated photo-crosslinking[88-92]. All of the crosslinking reactions start from the formation of tyrosyl radical, followed by diradical recombination with the other tyrosyl radical and enolization (Fig. 9).[93] The dityrosines are found in resilin, which has outstanding mechanical properties as an elastic protein and energy storage system.[89,94,95] It helps a cicada to produce the high frequency sound wave during the lifetime.[96] Therefore, there have been many attempts to introduce these mechanical properties into material engineering.[90,92,97-103] For example, dextran was conjugated with tyramine and elastic modulus of dextran-tyramine-based hydrogels was controlled by enzyme for biomedical application such as tissue engineering and drug delivery.[98]

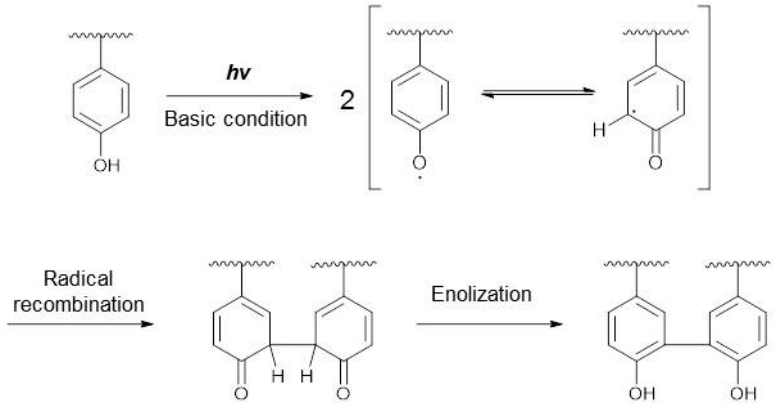

Figure 9. Mechanism of dityrosine crosslinking via proton abstraction, radical recombination, and enolization.

3. Research Objectives

In this thesis, bioinspired approaches using peptide or amino acid which are a powerful tool to diversify its structure and function are described. Among 20 amino aicds, tyrosine, which has folding and crosslinkable properties, was focused to investigate new roles in biomimetic applications.

In chaper 1, preparation of flower-like Pd nanostructure by using tyrosine-containing peptide as a template is described. The metal-peptide comlex induced self-assembly plays an important role in the formation of the flower-like Pd nanoparticles (NPs). The Pd NP capped with amphiphilic peptide was utilized for the copper-free Sonogashira reaction in water only solvent system.

In chapter 2, assembly of tyrosine-organic semiconductors using dityrosine crosslinkage at air/water interface was described. The perylene tetracarboxylic acid dianhydride (PTCDA) was modified with tyrosine, producing the Tyr-perylene diimide (PDI). The tyrosine was crosslinked by UV irradiation in aqueous basic condition, which led to the polymerization of PDI, affording an

amphiphilic molecule. The crosslinked Tyr-PDI was self-assembled into macroscopic and semi-crystalline nanofilm at air/water interface. Upon white light iradiation, this film gave a long-living photoconducting, and repeatable and prompt ‘on and off’ photocurrent switching properties.

Chapter I.
A Tyrosine-rich Peptide Induced Palladium Nanostructure for C-C Coupling Reactions

1. Introduction

1.1. Peptide as a Template for Synthesis of Metal Nanostructures

Nature determines protein structures by arranging amino acid sequences through genetic controls. The protein tertiary structures can control the exquisite sizes and morphologies of inorganic hybrid structures with high reproducibility under physiological conditions via so-called biomineralization process (Fig. 10).[104] For example, homogeneous iron oxide NPs (about 8~9 nm in size) are formed inside hollow polypeptide ferritin shells.[105] Not only the self-assembly of peptides but also the interactions between the peptides and metal ions are considered to be a key factor in forming organic-inorganic hybrid nanostructures (Fig. 11). By mimicking this biological process, various metal (Au,[106-108] Ag,[109-111] Pd,[112-114] Pt[115-117] and Cu[118,119]) NPs have been developed by using peptide templates with controllable geometrical, physical and chemical parameters (Fig. 12). However, understanding the design rule for peptide sequences

still remains a challenge.

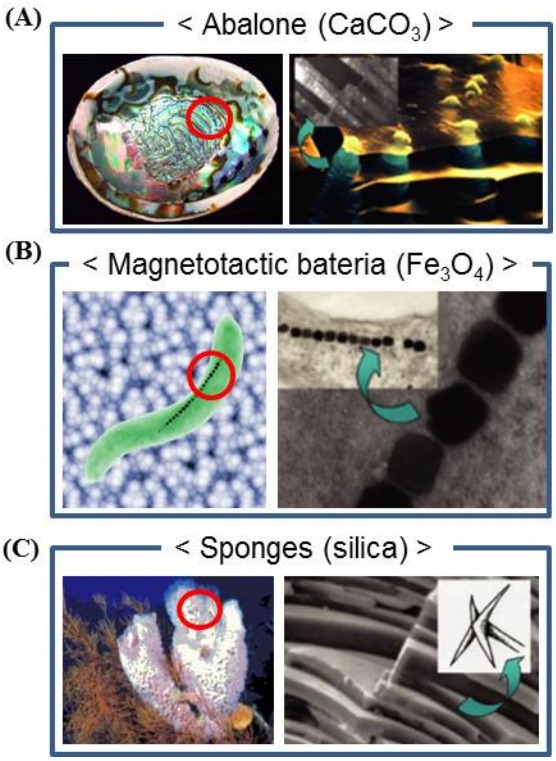

Figure 10. Examples of biomineralization.[18] (A) $CaCO_3$ laminates structure in abalone. (B) Crystallographically aligned Fe_3O_4 nanostructures formed by magnetotactic bacterium (*Aquaspirillum magnetotacticum*). (C) Layered silica structures observed in sponge spicule of Rosella.

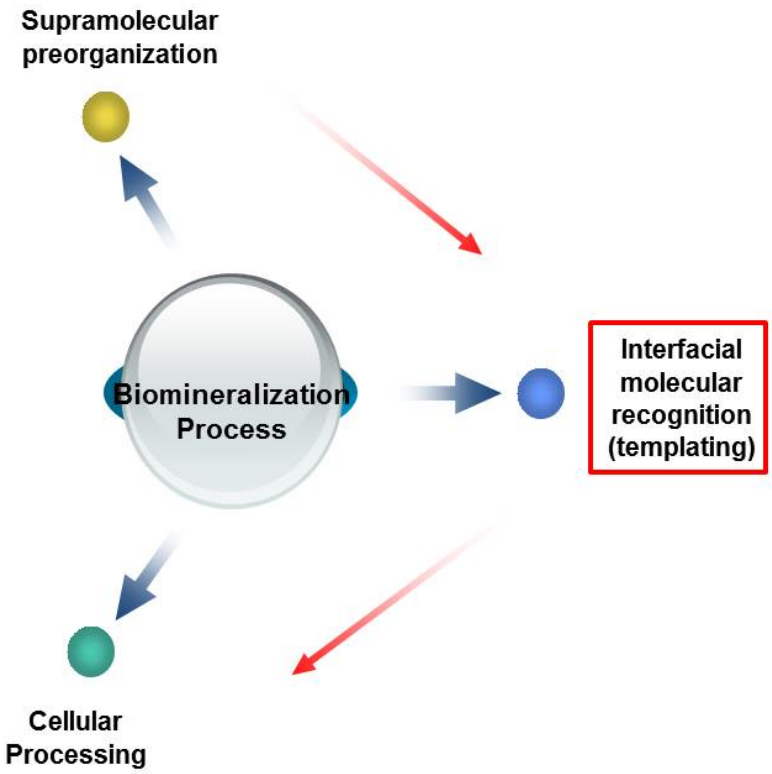

Figure 11. Scheme of biomineralization process.

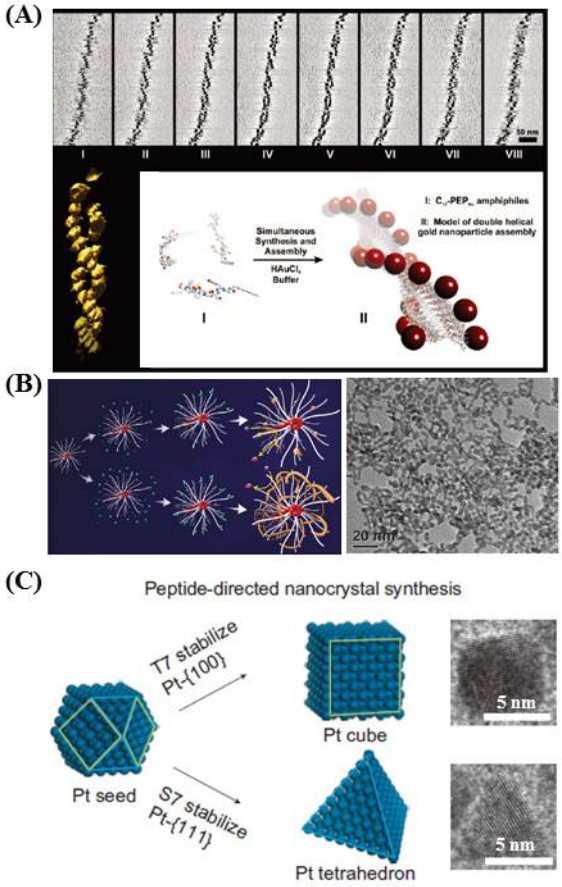

Figure 12. Examples of the synthesized nanostructures using biomimetic approach. (A) Sliced images of electron tomography data and schematic illustration of the formation of gold nanostructure.[106] (B) Synthetic scheme and TEM image of Pd NP network formed by R5 peptide template.[114] (C) Pt-(100) binding peptide sequence T7 and Pt-(111) binding peptide sequence S7 selected by phase display induce Pt cube and tetrahedron, respectively.[115]

1.2. Peptide-Templated Metal Nanomaterials as Heterogeneous Catalyst for Various Organic Reactions

Traditional homogeneous and heterogeneous catalysts used in large scale can produce toxic waste materials that necessitate specialized disposal means and require thermal activation, both of which might result in increasing production costs. Especially, with regard to the heterogeneous catalysts, their three-dimensional shape and surface property play an important role for giving high activity, because these factors can affect the accessibility of the reactants into the surface of catalysts. To control the morphology and the surface, a variety of templates such as dendrimers, polymers and micelles have been used for the fabrication of catalytically active metal nanomaterials. However, with increasing concerns about environmental protection and energy savings, many efforts to harness bio-inspired fabrication method, which is known as green process, by using peptides and proteins as a template have been reported. In

addition, green chemistry, which requires mild reaction temperature, water as a solvent and low metal loading, is attractive for catalytic reactions ranging from C-C bond formation to oxidation or reduction. Knecht and Naik groups used a phage display technique to find out specific peptide sequences that showed high binding affinity toward Pd, and used them as a template for Pd.[112] The specific peptide sequence (SSKKSGSYSGSKGSKRRIL), which has large numbers of lysine, was used as a template for Pd, based on the information that amine group has sequestrating and localizing property for metal ions.[114] Pd nanostructures fabricated by these peptide-templated approach catalyzed Stille reaction[112,114,120,121] and hydrogenation[121] in water based solvent at room temperature. In addition, peptide framework-related binding group/function or structure/function relationships for nanocatalysts were suggested.[120,121] Peptide-templated metal NPs developed by these methods may be useful in performing metal NP catalyzed organic reactions under physiological condition.

2. Experimental Section

2.1. Chemicals and Materials

2-Chlorotrityl chloride (CTC) (100-200 mesh, 1.26 mmol/g) resin, fritted polypropylene reactors (Libra tube RT-20M, 20 ml), Fmoc amino acids, 2-(1*H*-benzotriazole-1-yl)-1,1,3,3-tetramethyluronium hexafluorophosphate (HBTU), and hydroxybenzotriazole (HOBt) were purchased from BeadTech (Seoul, Korea). *N*,*N*-Diisopropylethylamine (DIPEA) was purchased from Alfa Aesar (Ward Hill, MA). Triisopropylsilane (TIPS), 3,6-dioxa-1,8-octanedithiol (DODT), anisole, sodium tetrachloropalladate (Na_2PdCl_4), ascorbic acid, iodobenzene, ethynyl pyridine, 1-ethynyl-1-cyclohexanol, 4-iodoanisole and phenylacetylene were purchased from Sigma-Aldrich (St. Louis, MO, USA). 1-Iodo-4-nitrobenzene was purchased from TCI (Tsukuba, Japan). Triethylamine (TEA) was purchased from Junsei (Japan).

2.2. Peptide Synthesis

The YYAHAYY peptide was synthesized on a 2-chlorotrityl chloride (CTC) resin (1.26 mmol/g) with Fmoc chemistry in a fritted reactor. After loading the first amino acid (0.3~0.5 mmol/g), each coupling step was performed with Fmoc-amino acid (2 eq), HBTU (2 eq), HOBt (2 eq) and DIPEA (4 eq) for 2 hours until the Kaiser-test was turned out to be negative. The mixture of DCM and DMF in a ratio of 1:1 was used as the solvent. The deprotection step of Fmoc group proceeded for 20 min by 20% piperidine/DMF. Cleavage of the final peptides from the CTC resin was conducted in 93% TFA, 2% TIPS, 2% DODT and 3% anisole for 90 min. The cleavage mixture was filtered and washed with DCM and methanol, and the filtrate was concentrated in vacuum. The resulting peptide residue was precipitated with cold diethyl ether, centrifuged, and dried in vacuum. The peptides were purified with reverse phase HPLC, when necessary, and identified by ESI mass spectrometer. The purity of the peptide was above 95%.

2.3. Fabrication of Palladium Nanoparticles

Pd nanoflowers were synthesized by the following method. A peptide stock solution (0.41 mg/ml) and a Na_2PdCl_4 stock solution (10 mM) were freshly prepared in every synthesis. For a total of 10 ml synthesis, 1 ml of the peptide stock solution was diluted with 6 ml of water. The Na_2PdCl_4 stock solution was injected into the diluted solution with the ratio of Pd:peptide 20. Additional water was injected to adjust the total volume (10 ml) equally. This mixture was vigorously stirred for 30 min at room temperature and then 1 ml of freshly pre-prepared reductant (50 mM ascorbic acid) was added. The reaction was carried out for 1 hr to form peptide assembly and sufficient reduction of Pd^{2+} ion. The resulting particles were centrifuged at 9000 rpm to wash out unreacted residues. This was repeated two more times. After supernatant was removed at the final centrifugation, 5 ml of water was added into the precipitant.

2.4. Characterization

UV/Vis Spectroscopy

Peptide/Pd^{2+} mixtures before/after reduction were characterized by Optizen 2120UV spectrometer (Mecasys) in a sample cell (Hellma Analytics, 10 mm pathlength). [Condition; room temperature, 0.5 nm intervals, 190 to 600 nm]

Circular Dichroism (CD) Spectroscopy

The CD spectra of peptide solution samples were recorded using a Chirascan™-plus CD detector (Applied Photophysics) in sample cell (Hellma Analytics, 0.05mm pathlength). The data from 5 scans were averaged for each spectrum. [Condition; room temperature, 1 nm intervals, 190 to 260 nm].

Fourier Transform Infrared Spectroscopy (FT-IR)

Peptide-containing samples were analyzed with a Agilent Cary660 FT-IR spectrometer equipped with an attenuated total reflection (ATR) accessory. Peptide-containing solution samples (80 ul) were deposited to a clean silicon wafer and dried under vacuum. The deposited samples on a silicon wafer were placed on a ZnSe/diamond for analysis. The scanned wave numbers ranged from 650 cm^{-1} to 4,000 cm^{-1} at a resolution of 2 cm^{-1}. The spectra were scanned 32 times.

Transmission Electron Microscope (TEM)

Each of the Pd NPs solution samples (20 ul) was deposited on a carbon-coated copper TEM grid (Ted Pella Inc., 300 mesh) and air-dried for 5 min. The remaining liquid was removed with a filter paper. The prepared TEM grids were kept in a desiccator before TEM and HR-TEM imaging to ensure the removal of moisture. The microscopic images were observed at 80 kV using TEM (JEOL, JEM 1010), and at 300 kV using HR-TEM (JEOL, JEM 3010).

Inductively Coupled Plasma-atomic Emission Spectroscopy (ICP-AES)

A Pd NFs aqueous solution was homogeneously dispersed using bath-type sonicator (Branson). The Pd NFs solution (100 ul) was injected into royal water (4 ml). After reaction for 8 hours at room temperature, the solution was diluted with DW. The concentration of palladium was quantified by ICP-AES (Shimadzu, ICPS-7500).

X-ray Diffraction (XRD) Analysis

A lyophilized Pd NFs sample was transferred to a sample holder. The XRD data were measured over a scattering angle ranging from 5˚ to 90˚ at 2θ step of 0.02˚ using CuK_{α} radiation with a diffracted beam monochromator in the reflection geometry at room temperature (Rigaku, Smart Lab).

2.5. Copper-free Sonogashira Reaction

The following procedure was chosen as a modified copper-free Sonogashira reaction.[122] The most effective base was chosen based on the preliminary experimental results. For each reaction, iodobenzene (0.5 mmol), phenylacetylene (0.6 mmol) and TEA (2.5 mmol) were added into a well-dispersed Pd nanoflower solution in 10 ml of total reaction volume. The mixture was stirred vigorously for 18 hr at 65-75 ℃. After the reaction, the reaction mixture was extracted with diethyl ether, small portion of the extracts were taken for GC-MS (Gas chromatography-mass spectrometry) analysis (equipped with a DB-5 capillary column).

3. Results and Discussion

3.1. Design of Peptide Template for Fabrication of Pd Nanostructure

A heptapeptide, Tyr-Tyr-Ala-His-Ala-Tyr-Tyr (YYAHAYY) (Tyr-H7mer, Fig. 13), was designed to synthesize Pd nanoparticles (NPs) under ambient conditions. In our previous study,[43] we reported that Tyr-containing peptides (YYACAYY) could be assembled into several nanostructures and at least two consecutive tyrosines were necessary for the peptide assembly. Tyrosine also has a potential as a bio-catalyst due to its redox active property.[123] To control the size and stability of Pd NPs, histidine was inserted at the center of the peptide sequence instead of Cys. Histidine can coordinate with several transition metal ions and nucleate the formation of metal NPs (Fig. 14).[120] Histidine, which is located between the two tyrosines, might control the size of Pd NPs by peptide folding. As it turned out, Pd NPs (4-5 nm size) with flower shapes were synthesized by Tyr-

H7mer in water.

Figure 15 illustrates a plausible mechanism for the formation of Pd nanoflowers (NFs) with Tyr-H7mer. Pd^{2+} ions are coordinated with His residues of Tyr-H7mer in water, resulting in peptide folding. The hydrophobic nature of the Tyr-H7mer/Pd^{2+} complex could accelerate the peptide assembly and at the same time the Pd^{2+} ions could be gradually reduced to Pd NPs.

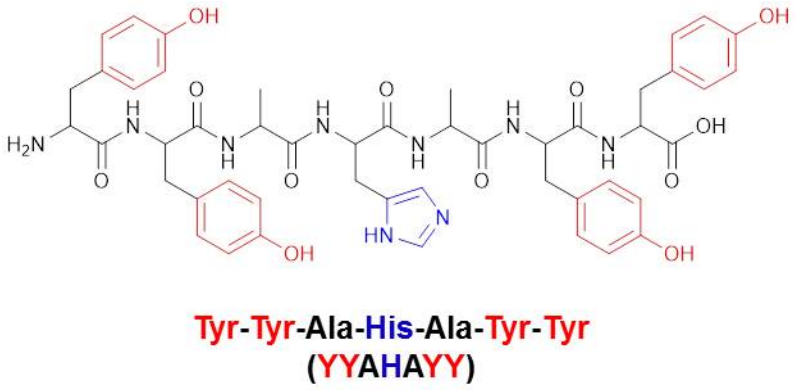

Figure 13. Chemical structure of YYAHAYY.

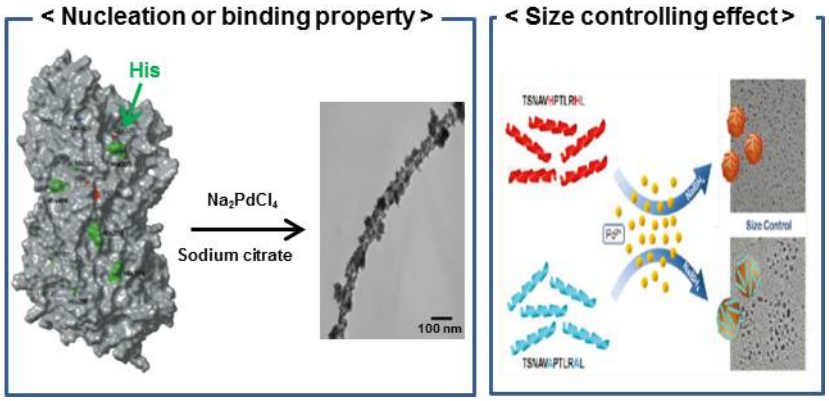

Figure 14. Importance of histidine (His) in the growth of Pd NPs.[120,124]

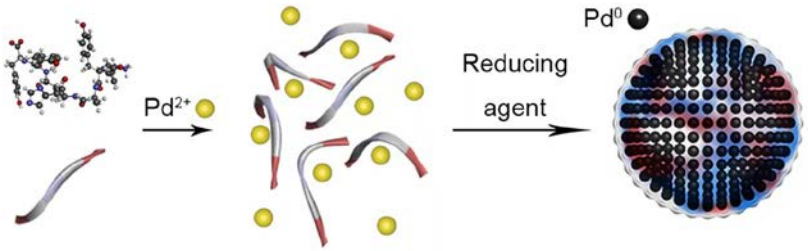

Figure 15. Schematic illustration for the formation of Pd nanoflowers (NFs) covered by peptides. Tyr-H7mers were coordinated with Pd ions and assembled. Then, Pd NFs were formed by reducing agent.[125]

3.2. Characterization of Tyrosine-rich Peptide Induced Flower-like Palladium Nanostructure

During the reduction process by ascorbic acid as a reducing agent, the color of the Tyr-H7mer containing Pd solution turned from pale yellow to dark brown. The UV/Vis spectra also showed the absorption changes during the formation of Pd NPs by Tyr-H7mer in water. As shown in Figure 16, the absorbance peak of Pd^{2+} at 207 nm gradually decreased and broadened during the formation of the Pd NPs.

Transmission electron microscopy (TEM) analysis revealed that uniform sized Pd NPs (4-5 nm) were assembled into flower-like shapes with the heptapeptides (Fig. 17A). The energy-dispersive X-ray spectroscopy (EDS) elemental mapping showed the distributions of Pd, N and O on the surface of Pd nanoflowers (NFs), which means that Pd NPs were capped with peptide template (Fig. 17B-E). Interestingly, the final morphologies of Pd NPs were dependent on the central amino acid in the peptide sequence. When His was substituted by Ala to give YYAAAYY

(Tyr-A7mer), irregular shaped Pd nano-aggregates were formed (Fig. 18). His could play an important role in peptide assembly with Pd^{2+} ions because the imidazole group of His can bind strongly with metal ions. Thus, histidine residue of the peptides provided the nucleation sites for Pd NFs formation before nucleation and growth of Pd NPs.[113] The sizes of Pd NFs were between 39 and 100 nm, with an average value of 66 nm ± 5 nm (Fig. 19). The Pd NPs could also be formed without adding any reducing agents. However, it took a very long time to form Pd NFs (4 weeks at room temperature) (Fig. 17F). This seems to be related to the weak reducing activity of Tyr residues.[126]

The Pd NFs were further characterized by high resolution transmission electron microscopy (HR-TEM) and powder X-ray diffraction (XRD) (Fig. 20). The lattice structure of a single Pd NP in the Pd NFs reveals the (111) plane of Pd (d-spacing at 0.23 nm) (Fig. 20B and Fig. 21). The Powder XRD pattern shows the crystallinity of Pd NFs. As shown in Figure 19C, peaks at 40.1°, 46.8°, 68°, 82.2°, and 86.4° correspond to the (111), (200), (220), (311), and (222) lattice planes of face-centered cubic (fcc) Pd.[127]

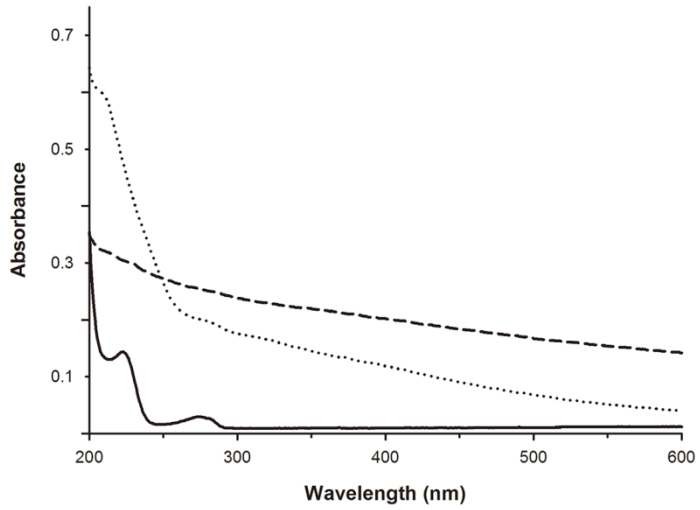

Figure 16. UV-Vis spectra of Tyr-H7mer (line), Pd^{2+}/Tyr-H7mer complex (dotted), and reduced Pd NFs prepared by the Tyr-H7mer (dash).[125]

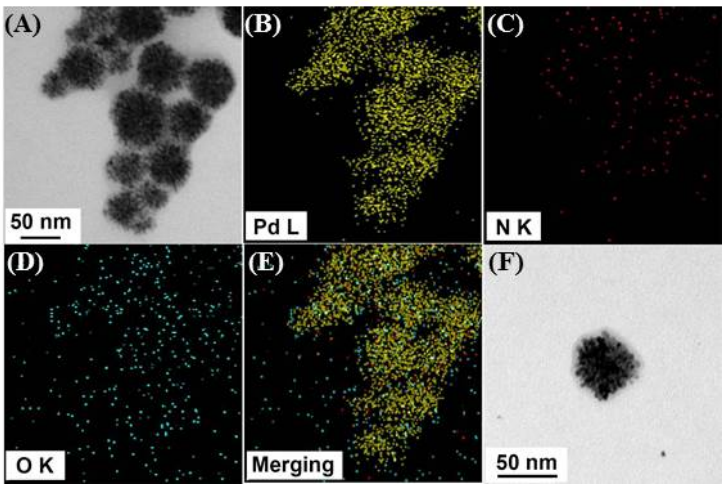

Figure 17. (A-E) HR-TEM/EDS mapping of Pd NFs. The homogeneous distributions of palladium (B), nitrogen (C), oxygen (D) and merged one (E). (F) TEM images of Pd NFs obtained by using the Tyr-H7mer as a template without reducing agent.[125]

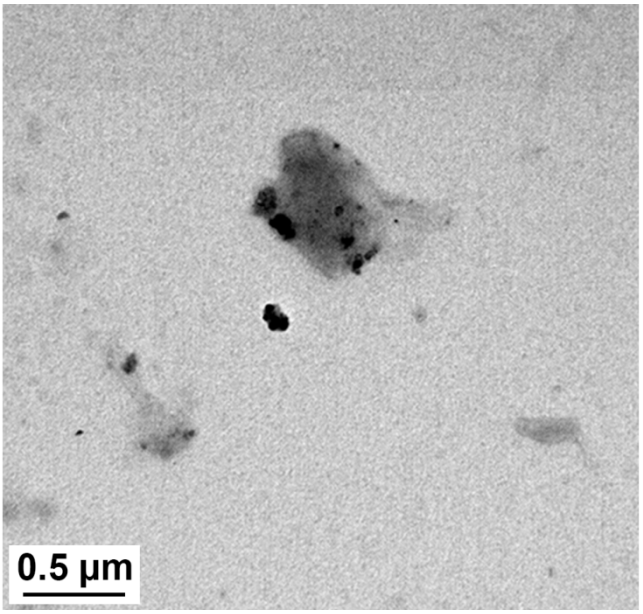

Figure 18. TEM images of Pd NPs prepared with YYAAAYY peptide.
125

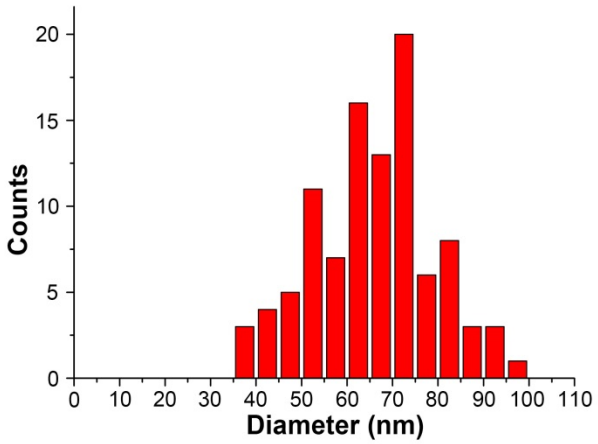

Figure 19. Size distribution histogram of Pd NFs.[125]

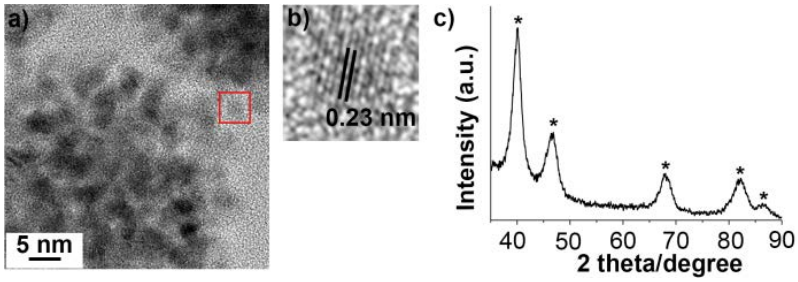

Figure 20. Crystalline property of Pd NFs. (A) HR-TEM image of Pd NFs. (B) HR-TEM image recorded from the particle (ca. 4 nm) marked by a red square in (A). (C) Powder XRD pattern of the Pd NFs. Pd peaks are indicated with a star (*).[125]

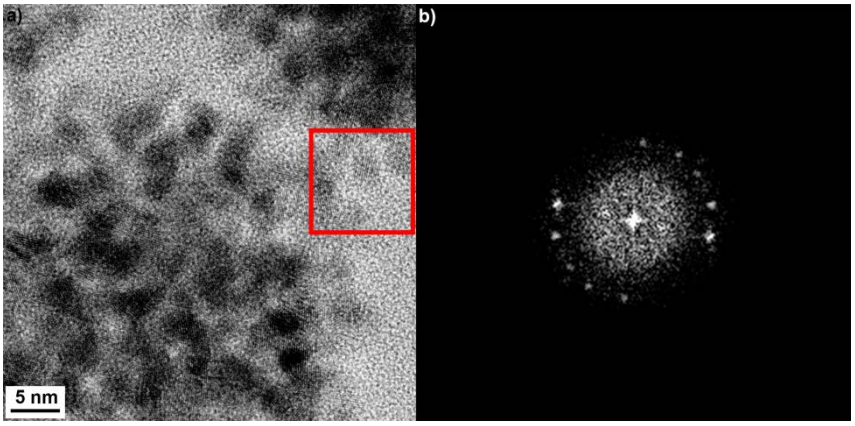

Figure 21. (A) HR-TEM image of Pd NFs and (B) electron diffraction pattern of the red square region in (A).[125]

The assembly mechanism for Tyr-H7mer during the formation of Pd NFs was studied by circular dichroism (CD) and Fourier transform-infrared (FT-IR) spectroscopy (Fig. 22). The richness of Tyr residues in the peptide sequence affected the entire pattern of the CD spectra.[43] The positive peaks at 202 and 227 nm are originated from the contributions of the phenolic side chains of the Tyr residues. After adding Pd^{2+}, the peak at 227 nm increased positively and was slightly red-shifted. The peak shifts of the Tyr residues indicate that Pd^{2+} ions are involved in peptide ordering.[128,129] The negative peak at 190 nm was reduced and shifted to 195 nm. It seems that the α-helical conformation of Tyr-H7mer is affected by Pd^{2+} mediated peptide assembly. In addition, the amide I band region (Fig. 22B, 1600-1700 cm^{-1}) was analysed to identify any conformational changes of the Tyr-H7mer during the assembly process.[130,131] As shown in Figure 22B, the α-helical peak at 1670 cm^{-1} was shifted to 1633 cm^{-1}, which corresponds to the β-sheet structure. After the reduction of Pd^{2+} ions, the 1633 cm^{-1} peak was shifted slightly to 1628 cm^{-1}.

We could also confirm the interaction between the His residue

and the Pd^{2+} ion by analysing FT-IR spectra of various protonated forms of the His side chain (imidazole group).[132] The His peak ($HisH_2^+$) at 1635 cm^{-1} of free Tyr-7Hmer in water was shifted to 1578 cm^{-1} after the formation of Pd NFs, indicating that one proton was removed from $HisH_2^+$. Afterward, the reduction of Pd^{2+} ions caused the peak to further shift to 1562 cm^{-1}. It may be possible that the His residue interacts with the closest His residue in the vicinity to produce dimers connected by hydrogen bonds. Considering all these, it can be conclued that the Tyr-H7mer acted as a template for organizing the Pd^{2+} ions to form Pd NFs.

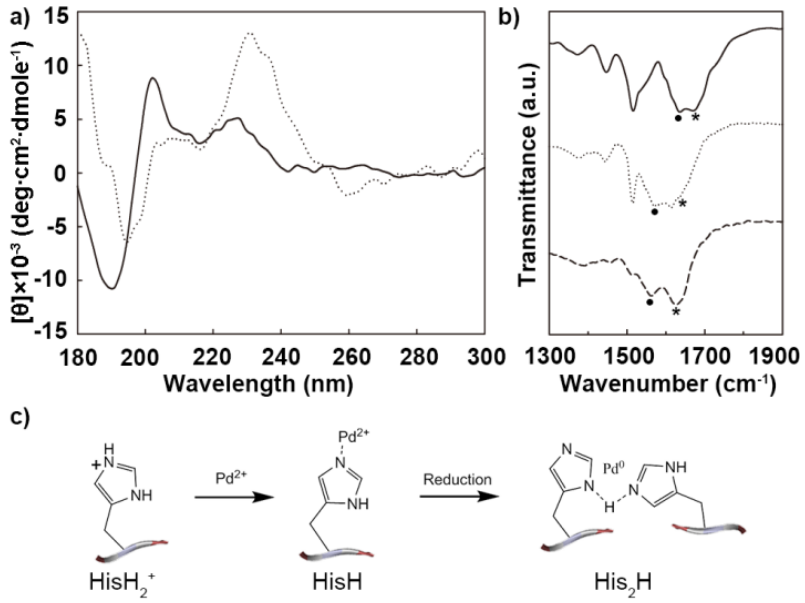

Figure 22. Spectroscopic data for confirming peptide structural changes. Peptide, Pd2+/peptide complex, and reduced Pd NFs are indicated by line, dotted line, and dash line, respectively. (A) CD spectra of Tyr-H7mer in each steps (B) The FTIR spectra of Tyr-H7mers in each step. Amide Ⅰ band peaks are marked with star (*). Histidine-related peaks are marked with circle (•) (C) Proposed mechanism based on FTIR data focusing on the interaction between Pd^{2+} ion and histidine residue of the peptide.[125]

3.3. Catalytic Properties of Palladium Nanoflower in Copper-free Sonogashira Reaction

For atom efficiency and sustainability, a mild reaction condition for the Sonogashira cross-coupling reaction without using Cu(I) co-catalysts and phosphine ligands has been pursued. Fortunately, the Pd NFs have an ideal property as a catalyst for the Sonogashira cross-coupling reaction under ambient aerobic conditions; accelerating oxidative addition step of Pd^0 with aryl halide by peptide ligand having steric and proper electronic property,[133] and enhancing the formation of arylalkynylpalladium species[134].

First, the reaction conditions of iodobenzene and phenylacetylene was optimized in order to avoid the loss of Pd and maximize the catalytic efficiency; the amount of catalyst and the reaction time (Fig. 23). At room temperature, the yield was logarithmically increased with the amount of catalyst and 0.5 mol% of Pd NFs was almost the saturation point. Then, by fixing the amount of Pd NFs as 0.5 mol%, the reaction kinetics was

followed at 65 °C, which revealed that after 18 hr to 24 hr, similar yields was obtained. Taken together, 0.5 mol% of Pd NFs, 18 hr, and 65 °C were selected as the optimal reaction conditions in water.

As shown in Table 1, a copper-free Sonogashira cross-coupling reaction catalyzed by Pd NFs was successfully performed in an aqueous condition. Coupling reactions of iodobenzene with two different alkynes (1-phenylacetylene and 1-ethyne-1-cyclohexanol) generated the corresponding products in 96 % and 81 % yields, respectively (entries 1 and 2). This catalytic system worked very well even though electron withdrawing substituents exist in the phenyl ring for the coupling reaction (entry 3). Three types of aryl iodides were reacted with phenylacetylene, producing the corresponding cross-coupling products in high yields over 93 % (entries 1 and 3, 4). Furthermore, the Pd NFs performed well in coupling reactions with heteroatom containing alkyne affording high yield (entry 5). Thus, we proved that the Sonogashira cross-coupling reaction was widely tolerable with various aryl iodides in water system. These results are in good

agreement with the previous reports that stabilizer and supporting materials around Pd^0 can prevent undesired aggregates and improved catalytic performance.[135] In addition, the Glaser-type oxidative homocoupling side-reaction could be avoided due to not using copper salt. These results exhibit that the Pd NF heterogeneous catalyst is better than the previously reported ones (Table 2). The Pd NFs catalyst showed the turnover frequency (TOF) of 11 for the Sonogashira coupling reaction between iodobenzene and 1-phenylacetylene. In Table 2, Moreover, under the present catalytic system, no additive was necessary, and the reaction proceeded smoothly at moderate temperature of 65 °C in water. The excellent catalytic activity of the Pd NFs would be attributed to the "Breslow effect" [136-138] in water by their amphiphilic property.

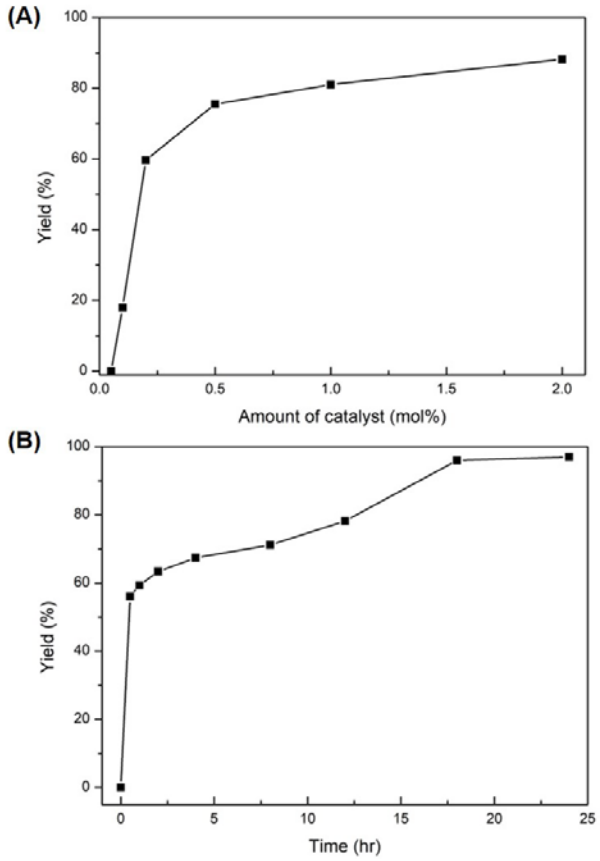

Figure 23. Optimization of the reaction conditions. (A) the amount of catalyst and (B) the reaction time.

Table 1. Aqueous Copper-free Sonogashira Cross-coupling Reaction using Pd NFs[a]

Entry	Aryl halide	Alkyne	Product	Yield[b] (%)
1		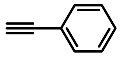	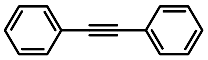	96
2		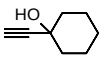	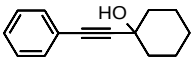	81
3	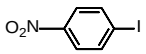	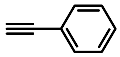	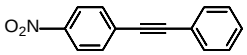	97
4	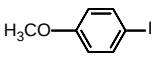	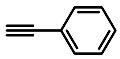	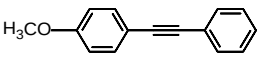	93
5		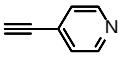	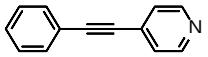	82
6[c]		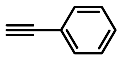	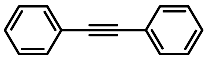	98

[a] Reactions were performed using 0.5 mmol substrate, 2.5 eq. triethylamine, and 0.5 mol% Pd NFs in water (10 mL).[b] Determined by GC-MS through corrected normalized peak areas.

[c] Pd/C was used as a catalyst.

Table 2. Comparison of the Activity of Pd NF Catalyst with Other Heterogeneous Pd catalysts in C-C Coupling of Iodobenzene with Phenylacetylene

Catalyst (mol% of Pd)	Conditions	Time (h)	Yield (%)	TOF (h^{-1})	Ref
Pd/MPC (1 mol%)	H_2O, CuI, PPh_3, TEA, 60 ℃	24	100	4	Catal. Lett., 146 (2016), 1792-1799
Pd-dendrimer-Si NPs (0.4 mol%)	H_2O, K_2CO_3, Reflux	3	32	27	Appl. Organometal. Chem., 30 (2016), 657-663
Pd/L/Fe_2O_3 NP (0.18 mol%)	H_2O, TEA, 60 ℃	24	52	12	Appl. Catal. A Gen., 525 (2016), 31-40
β-CD/Pd NPs (10 mol%)	H_2O, DIA, r.t.	20	89	0.4	Catal. Lett., 116 (2007), 94-99

3.4. Recycling of Palladium Nanoflower

To determine the structural stability of the Pd NFs catalyst over reaction time, TEM images were obtained after the reactions. As shown in Figure 24, the Pd NFs remained structurally stable after the copper free Sonogashira cross-coupling reaction for 18h. To further prove this, FT-IR and XRD analysis were conducted (Fig. 25). After the reaction, the β-sheet conformation of Tyr-H7mer was maintained, verified from the 1628 cm^{-1} peak. In addition, the crystallinity of Pd NFs remained almost unchanged.

The Pd NFs catalyst maintained the high catalytic performance after fourth recycling for the coupling reactions. Substantial loss was not observed after fouth rounds of the catalyst recovery. Figure 26 shows that the yields of the corresponding product for the reaction of iodobenzene and 1-phenylacetylene were 96% (1^{st} run), 93% (2^{nd}rund), 91% (3^{rd} run), and 92% (4^{th} run).

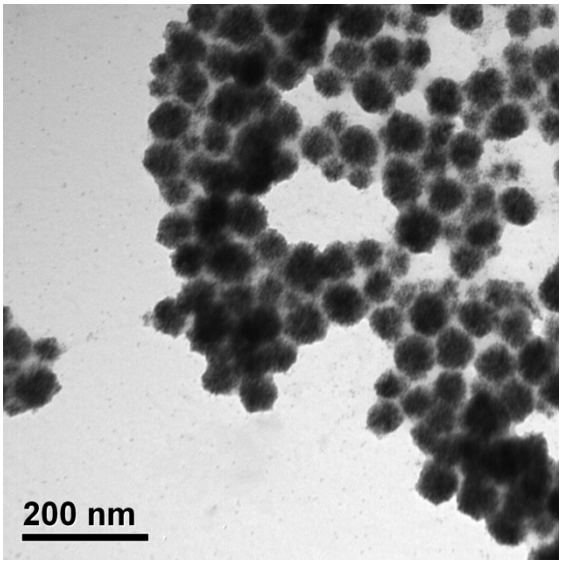

Figure 24. TEM image of Pd NFs after copper free Sonogashira cross-coupling reaction.[125]

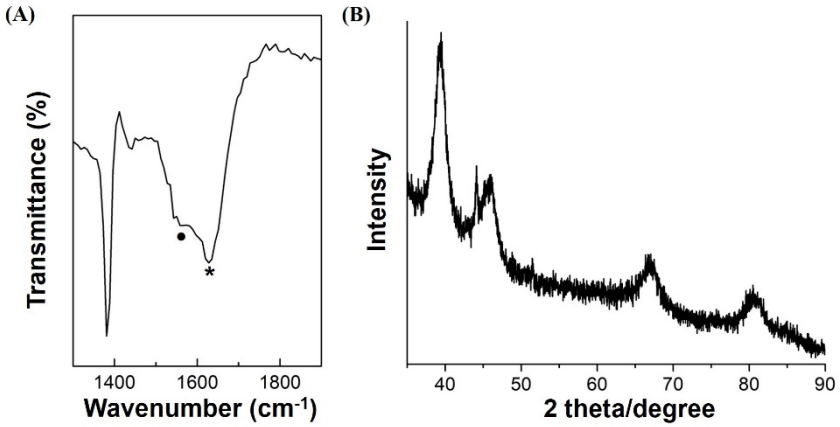

Figure 25. Characterization of Pd NFs after 1st run of copper-free Sonogashira cross-coupling reaction. (A) FT-IR, and (B) XRD data

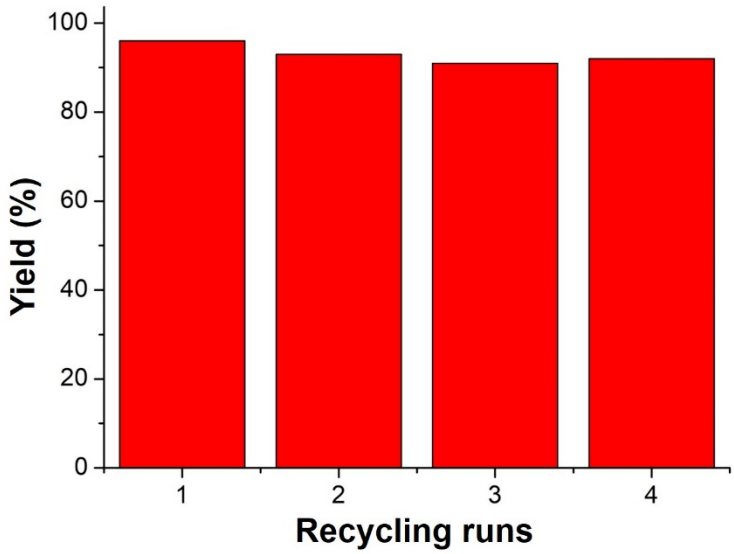

Figure 26. Yields after recycling Pd NF catalyst in water.

3.5. Mechanism of Efficient Catalytic Activities of Palladium Nanoflower in Water

By BET anlaysis, we found that the surface area and the pore volume of the Pd NFs were 20.5 m^2/g and 3.4×10^{-5} cm^3/g, respectively, which were much lower than those of Pd/C (S_{BET} (m^2/g) : 671.6, V_P (cm^3/g) : 0.17). Generally, the surface area is the dominant factor in controlling catalytic activity of heterogeneous catalyst. Having ~30 times lower surface area, the catalytic performance of Pd NFs was almost identical to Pd/C. This outstanding results may come from the amphiphilic nature of Pd NFs as mentioned in Chapter 3.3. The amphiphilic peptide template can increase the accessibility of hydrophobic substrates to the Pd NPs in water.

4. Conclusion

A simple method for preparation of Pd nanostructure with a flower-like morphology was presented by using Tyr-H7mer peptide as a template. The peptide folding and the interaction of Pd^{2+} ions with His residues in the Tyr-H7mer peptide are the crucial factors for the nucleation and growth of Pd NPs into the Pd NFs. The Pd NFs were very reactive and reusable catalyst for copper-free Sonogashira cross-coupling reactions in an eco-friendly water solvent system without collapse of their structure. Controlling the morphology of metal NPs by redox active peptide is a novel method to fabricate a new type of metal-peptide hybrid catalysts.

Chapter II.
Covalent Self-assembly of Tyrosine-appended Perylene Diimides for Photocurrent Generation

1. Introduction

1.1. Perylene derivatives and their Properties

Perylene tetracarboxylic acid dianhydride (PTCDA) is a versatile organic chromophore which draws much attention as in electronic materials which can be utilized in organic field effect transistor[139,140] and artificial light harvesting systems[141-143] due to its high molar absorptivity, high quantum yields and electron accepting property (n-type semiconductor). However, its extreme insolubility in organic solvents impedes solution based applications. Therefore, in order to increase the solubility in organic solvent, the anhydride position of the PTCDA has been functionalized into the corresponding imines, which are called as perylene tetracarboxylic acid diimide (PTCDI or PDI, Figure 27), through $Zn(OAc)_2$-catalyzed dehydration reaction with various aromatic and aliphatic amines. This perylene-based chemistry was developed by Langhals's group and BASF company.[144] In addition, by introducing Br or Cl atoms into the bay position of the perylene core, it is possible to expand its molecular designs

and functions.[145-148]

Functionalization on the imide- or -bay position has an effect on the optical and redox properties of the PDI.[149] PDI shows the slightly shifted absorption and fluorescence band with high quantum yields (>0.9) in the majority of solvents except for protic solvents, compared to the perylene that originally has the UV/vis absorption band from ~440 to ~525 nm and its mirror fluorescence band. The electron withdrawing property of the imide make the electron cloud of the perylene core dispersed to the imide at both sides, resulting in the electron deficient state of the PDI. In the same context, tuning the bay position is easy to control the properties of the PDI than doing on the imide position. For example, electron-withdrawing and electron-donating groups as a substituent of the perylene core can give a strong influence the maximum absorption wavelength and the molecular orbitals (Fig. 28).

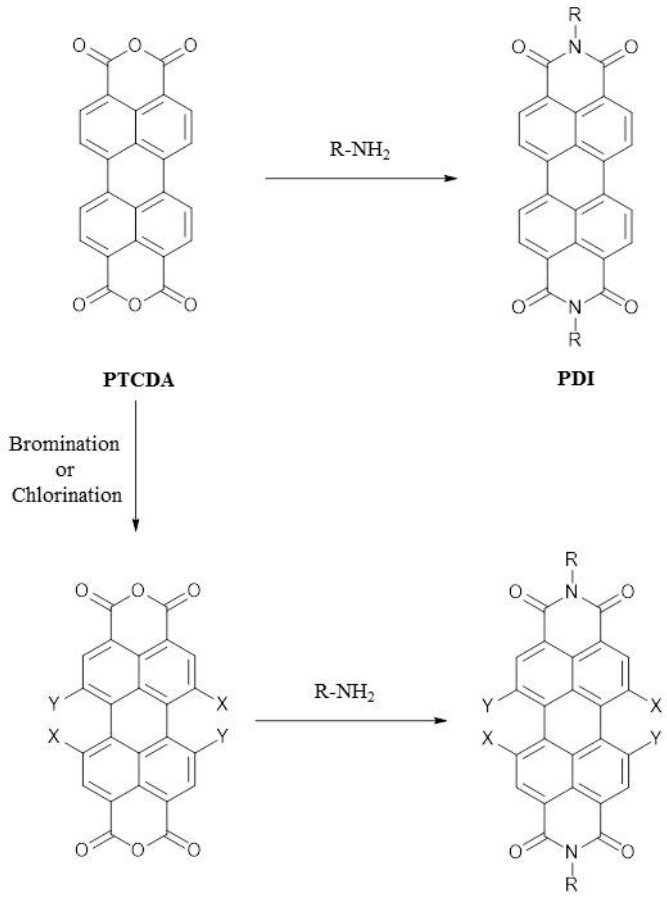

Figure 27. Modification of PTCDA. (R=alkyl, benzene; X=Br or Cl; Y =H or Cl)

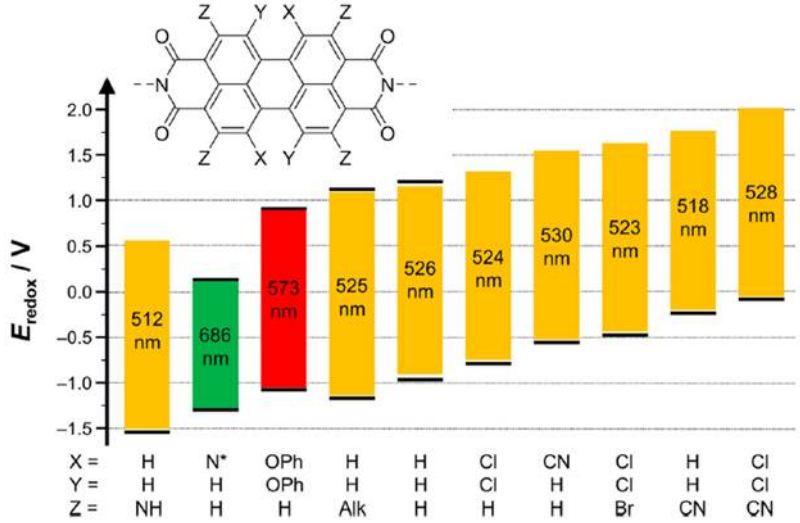

Figure 28. Effect of various bay-functionalizations on the optical and redox properties of the PDI.[149]

1.2. Packing and Self-assembly of Perylene Diimides

PDI have a strong tendency to self-assemble into 1-D stacked structure and its stacking is strongly influenced by the electronic interactions of building blocks. Such stacking can be followed by the colour changes resulting from mutual interactions between perylene cores depending on the different substituent-induced packing. This was suggested through empirical correlations by Graser, Hadicke and Klobe.[150-154] For example, PDIs having azobenzene, methyl and phenethyl substituents at the imide nitrogens are differently packed, resulting in brilliant red, maroon and black colours, respectively (Fig. 29). Through modification of the imide- or bay-position of the PDI, diverse self-assemblies can be induced. Each of the pi-stacked distances between adjacent perylene cores is between 3.34 and 3.55 Å. In the case of bay-modified PDIs, the substitution leads to the breaking of symmetry, resulting in two atropisomers (M/P-dimeric units) and the difference of the packing pattern between the PDIs (Fig. 30).

This distorted non-planar structure generates a lot of variations to be considered for making well-defined PDI structures. The well-defined self-assembled structures from the PDI derivatives can be directly correlated to their charge transporting property.

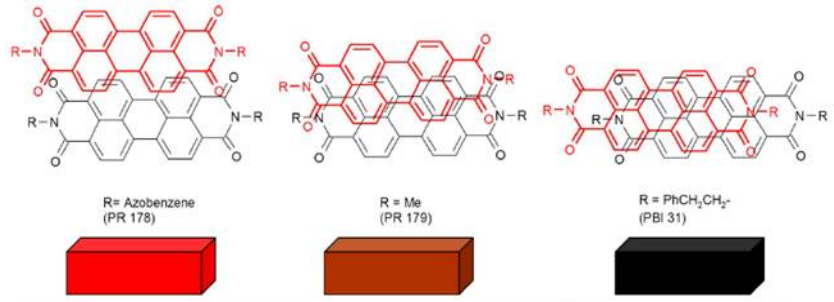

Figure 29. Color changes depending on the substituents at the imide position of PDI.[149]

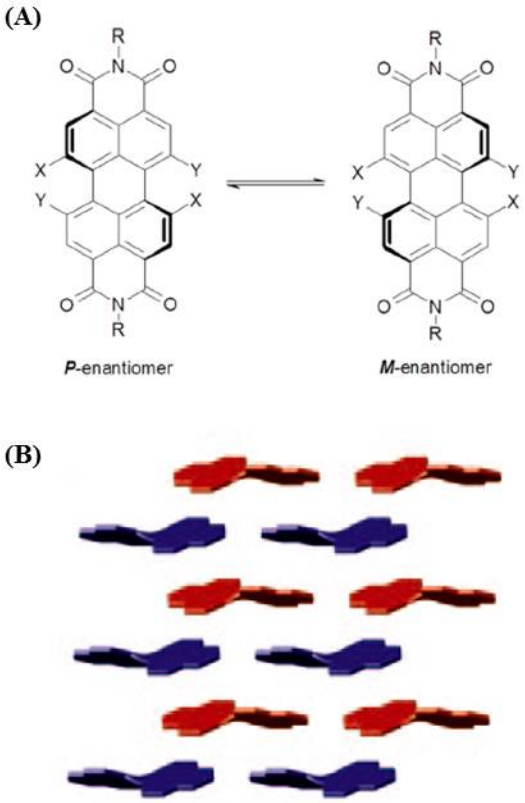

Figure 30. Molecular structure and packing of the bay position-modifed PDI. (A) Possible enantiomers created by modification of bay positions of the PDI.[155] (B) Packing mode of the distorted bay-modified PDI.[156]

1.3. Perylene Diimides as an Efficient Photocurrent Generator

PDI derivatives are one of the efficient light harvesting organic molecules due to its air-stable n-type property. One of the strategies to use the PDIs as an efficient photocurrent generator is to design well-packed structures, in which electron donors are covalently or non-covalently linked to the PDI core (electron acceptor). This structure can draw efficient charge separation upon photoexcitation.[157-159] Slow charge recombination as well as efficient charge separation is an essential prerequisite for high photoconductivity.[160] These factors can be manipulated by selecting the electron donors which have slightly higher HOMO level than PDI's HOMO level and controlling the distance between electron donor and acceptor. Based on this, several examples which have electron donating groups appended to the electron accepting PDI molecules have been reported.[161,162] For example, the PDI-derivatives having *N*,*N*-dimethylaniline as an electron donor showed a good kinetic balance between the

intramolecular charge recombination and the intermolecular charge transport along the stacked PDIs.[161]

2. Experimental Section

2.1. Chemicals and Materials

L-Tyrosine was purchased from Sigma-Aldrich (St. Louis, MO, USA). 3,4,9,10-Perylenetetracarboxylic dianhydride (PTCDA), *N*-cyclohexyl-3-aminopropanesulfonic acid (CAPS) and imidazole were purchased from Alfa Aesar (Ward Hill, MA, USA). Hydrochloric acid (HCl) were purchased from Dae-Jung Chemicals (Gyeonggi-do, South Korea).

2.2. Synthesis of Tyrosine-conjugated Perylene Diimide

In a 100 mL round bottom flask, *L*-tyrosine (362 mg, 2 mmol), PTCDA (392 mg, 1 mmol) and imidazole (5 g) were charged. The mixture was then purged with argon gas for 10 min before being heated at 130 ˚C overnight. The heating was maintained under an argon atmosphere. Then, the reaction mixture was cooled to 90 ˚C. Deionized water was added to the mixture under argon atmosphere, and then it was left for 1 h. The dark red solution was filtered to remove trace amount of unreacted PTCDA. The solution was then acidified with 2 M HCl aqueous solution until the pH of the mixture reached 2. Then, the acidified solution was centrifuged for 30 min at 7000 rpm. Supernatant solution was decanted and deionized (DI) water was added to neutralize the product. This centrifugation process was repeated two more times. After that, dark red precipitate was obtained by vacuum filtration. It was then dried overnight in air.

Yield: 696.7 mg (0.92 mmol, 92%). ^{1}H NMR (400 MHz, DMSO-

d_6, 25 ℃): δ = 13.07 (br, 2H; -COOH); 9.08 (s, 2H); 8.26 (s, 8H); 7.06 (d, J=8 Hz); 6.58 (d, J = 8 Hz); 5.92 (m, 2H); 3.53-3.35 (m, 4H). ESI-MS: m/z: calculated for $C_{46}H_{32}N_4O_{12}$: 832.20; found: 831.0 [M -H].

2.3. Self-assembly of Tyrosine-conjugated Perylene Diimides by Dityrosine Crosslinking

Tyrosine-conjugated PDI was solubilized in 0.1 M CAPS buffer (pH 10). This solution was poured into proper container (Petri dish or beaker). UV irradiation was performed on the surface of the solution. Then, photo-crosslinked PDI film was formed on the air-water interface. For transfer of the photo-crosslinked PDI film, a substrate was put in the reaction container before adding the reaction solutions, and then a solution of Y-PDI in 0.1 M CAPS buffer (pH 10) was poured into the reaction container to make the surface of the solution 10 mm higher than the substrate. After the crosslinked film was formed, the subphase was removed from the container with a syringe to make the film deposition on the substrate when the air-water interface passed through the substrate.

2.4. Characterization

Nuclear Magnetic Resonance (NMR) Spectroscopy

The dityrosine crosslinked PDI film-containing solution was purified by dialysis for a week using a dialysis tubing (MWCO: 1000 Da). The dialyzed solution was lyophilized, and re-dissolved in 1 ml of DMSO-d6 (Cambridge Isotope Laboratories, Andover, MA, USA). All NMR spectra were recorded on a Bruker Avance 500 MHz spectrometer. 2D experiments were performed using rotating-frame nuclear Overhauser effect correlation spectroscopy (ROESY). ROESY experiment was performed using 700 ms spin lock mixing pulses. 2D spectrum was recoreded on a Bruker Avance 600 MHz cryo-NMR spectrometer.

UV/Vis Spectroscopy

Samples before/after UV induced self-assembly were characterized by Optizen 2120UV spectrometer (Mecasys) in

sample cell (Hellma Analytics, 10 mm pathlength). [Condition; room temperature, 1.0 nm intervals, 250 to 600 nm]

Fluorescence (FL) Spectroscopy

Samples before/after UV induced self-assembly were characterized by LS-55 FL spectrometer (PerkinElmer, Waltham, MA, USA) in a sample cell (Hellma Analytics, 10 mm pathlength). [Condition; room temperature, 0.5 nm intervals]

Transmission Electron Microscope

PDI film solution (20 ul) was deposited on a carbon-coated copper TEM grid (Ted Pella Inc., 300 mesh) and air-dried for 5 min. The remaining liquid was removed with a filter paper. The prepared TEM grids were kept in a desiccator before TEM and HR-TEM imaging to ensure the removal of moisture. The microscopic images were observed at 80 kV using TEM (JEOL,

JEM 1010), and at 120 kV using HR-TEM (JEOL, JEM 3010).

X-ray Diffraction Analysis

Crosslinked floating film solution was transferred to a dialysis tubing (MWCO 1000) and dialyzed in DI water to remove the remaining buffer salt for a week. The washed film solution was lyophilized and was transferred to a sample holder. The XRD data were measured over the scattering angle ranging from 5˚ to 90˚ at 2θ step of 0.02˚ and scanspeed of 0.5 sec/step using CuK_{α} radiation with a diffracted beam monochromator in the reflection geometry at room temperature (Bruker, D8 ADVANCE with DAVINCI).

Transient Absorption Spectra

To analyze transient absorption (TA) spectra, PDI-Y solutions in 0.1 M CAPS buffer (pH 10) before/after 4 hr of UV-irradiation

were used. A femtosecond pulse (130 fs, 120 cm^{-1}, 650 μJ, 1 kHz) centered at 800 nm was generated by a standard regenerative-amplified Ti:sapphire laser (Hurricane, Spectra Physics). Continuum light, which was used as the probe pulse, was generated by focusing 800 nm light using a planoconvex lens (f = 10 cm) into a sapphire plate (WG31050, Thorlabs). The pump pulses were generated using a second harmonic generator (TP1A, Spectra Physics). The optical time delay between the pump pulse and the continuum pulse was scanned using a delay stage (Daedal 404300XRMP, Parker). The pump pulses were modulated using a synchronized optical chopper (MC1000, Thorlabs). The probe pulses of the signal were detected by photodiodes (2031, New Focus) after wavelength selection using a monochromator (model 250 is/sm, grating of 600 grooves blazed at 730 nm, Chromex). The temporal profiles of the TA were obtained using a lock-in amplifier (SR830, SRS).

Photocurrent Measurement

Photocurrent measurements of the crosslinked PDI-Y films were carried out through a simple two-probe method using a probe station with a CCD camera for in situ imaging of the device and Agilent B1500A semiconductor parameter analyzer for high-resolution current measurement. The interdigitized electrodes (IDEs) were fabricated by photolithography on a quartz glass, where AZ 5214E photoresist and mask-less photo-lithographer were used. A 5 nm of Cr and 50 nm of Au electrodes were then sputtered in order on the substrate with DC sputter (Channel dimension : 200 μm x 10 μm). After the deposition process, unwanted parts of the electrodes were removed by lift-off process. A tungsten lamp (500 W of input power, Newport) was used as the light source. The light was guided by a fiber (MS Tech) to excite the crosslinked PDI-Y films. The photocurrent measurements under vacuum were performed in a homemade chamber that houses the crosslinked PDI-Y film on the IDE quartz. The power of the whitelight which approaches to the crosslinked PDI-Y film was 4.42 mW/cm2.

3. Results and Discussion

3.1. Preparation of Crosslinked Free-floating Tyrosine-PDI Film

For covalent self-assembly, bola-amphiphilic tyrosine-appended perylene diimide (Y-PDI) was synthesized by zinc-catalyzed dehydration reaction between perylene tetracarboxylic acid dianhydride (PTCDA) and α-amino group of tyrosine, based on the previous method.[144] Using dityrosine linkage induced by UV (300 nm) irradiation at pH ≥ 10, Y-PDIs were directly polymerized and assembled at air/water interface by covalent bonding and pi-pi stacking, respectively. Interestingly, the resulting film could be observed with naked eye on the air/water interface in less than 2 h of UV (300 nm) frontal irradiation onto the surface of the Y-PDI solution (1 mg/ml) in 0.1 M CAPS buffer (pH 10) in a glass Peteri dish (35 * 10 mm) (Fig. 31A). The scale of the film could be expanded to a larger size (87 * 15 mm, Figure 31B). This result can be obtained at various concentrations of Y-PDI above 0.1 mg/ml (0.14 mM).

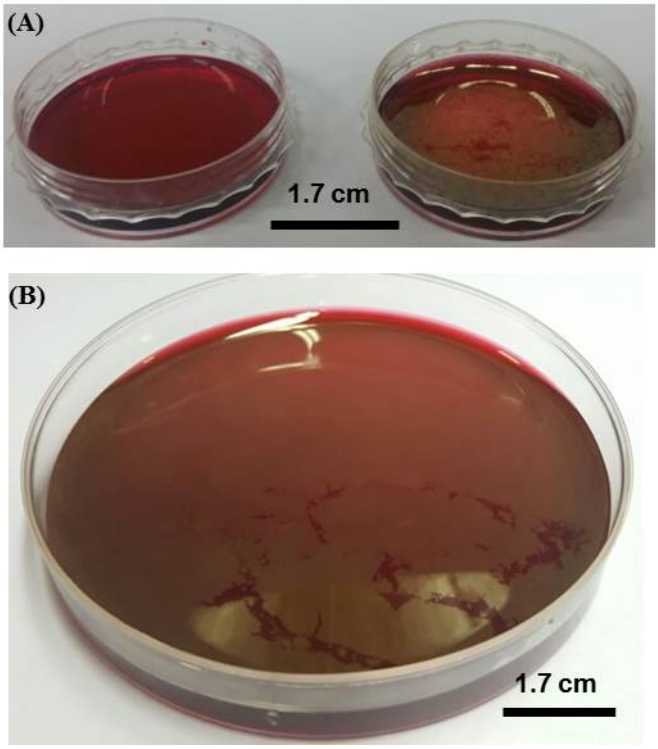

Figure 31. UV crosslinked PDI film at the air/water interface. (A) Optical images of Y-PDI solution without UV 6 hr (left), and with UV 6 hr (right). (B) Large size crosslinked PDI film formed at the air/water interface.

3.2. Characterization of Crosslinked PDI Film

Microstructure of the PDI film was observed by using transmission electron microscopy (TEM, Fig. 32). The minimal UV-irradiation time for the film formation was about 3 min, and thin nanosheets started to form. After 3 min, the darkness of the film gradually increased, which maybe related to the increase of film thickness. As the result, large sized PDI sheets with several micron-sized area were obtained (Fig. 32D). Atomic force microscopy (AFM) also shows that the film on the air/water interface has the flat and uniform surface in microscopic scale (Fig. 33A) and the aggregated and entangled structure can be seen in nano-scale (Fig. 33B). This aggregated structures were occasionally discovered in semi-crystalline polymer films.[163]

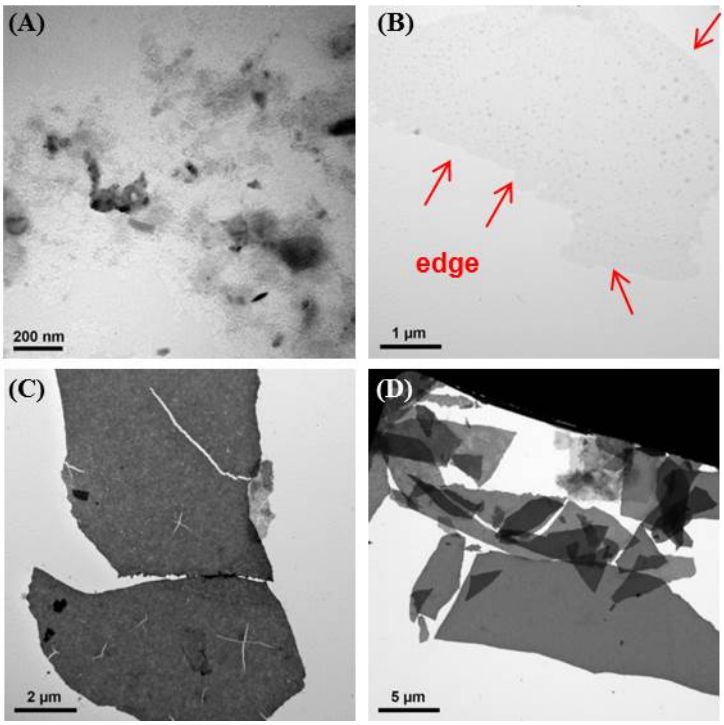

Figure 32. TEM images of crosslinked PDI film depending on UV-irradiation time ((A) 1 min, (B) 3 min, (C) 30 min, (D) 1 hr).

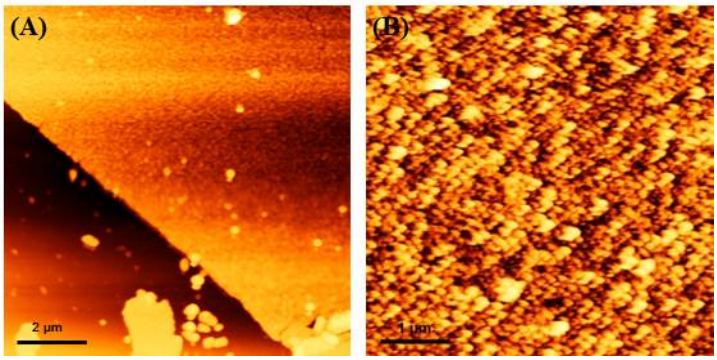

Figure 33. AFM images of crosslinked PDI film. (A) 10 um * 10 um scale (B) 5 um * 5 um scale

Figure 34 shows the photopolymerization kinetics (thickness vs time) at air/water interface. The Y-PDI films formed at 1 mg/ml concentration were initially thin (0.8 nm), and then, logarithmically grew to ca. 47 nm of thickness with increasing irradiation time. This curve represents a typical pattern for the crosslinked photopolymerization.[164] In this case, a fast instantaneous UV-initiated polymerization and assembly occur at the early stage. Once the interfacial film is thickened to a certain level, penetration of UV into the solution phase starts to decrease and the thickness of the photocrosslinked film is limited ca. 47 nm.

To investigate the formation of dityrosine (diTyr) crosslinkages and its effect of self-assembly behaviour of the crosslinked Y-PDI, the self-floating film was analysed using spectroscopic analysis. The absorption spectra (Fig. 35A) of the Y-PDI aqueous solution in 0.1 M CAPS buffer (pH 10) exhibited a weak tyrosine ring peak at ~280 nm and the perylene core-related peaks at 477, 508 and 545 nm which correspond to 0-2, 0-1 and 0-0 vibrational modes.[165,166] When UV irradiation time was increased, a peak at

330 nm was increased, which might result from the gradual formation of diTyr linkage.[82,167] In the region of 450-600 nm, broadened and slightly red shifted peaks were observed due to the formation of a band structure arising from specific interactions between the stacked PDI pi-systems.[166,168] The UV spectra of the film state transferred to a quartz substrate showed that the lowest energy absorption peak at 545 nm was red-shifted to 564 nm (Fig. 36). Furthermore, the time dependent fluorescence emission supports the formation of diTyr crosslinkages and the PDI stacking. Under 330 nm excitation, the diTyr peak intensity of 430 nm increased until the UV irradiation of 2 h, and then, the intensity was decreased due to self-quenching by pi-pi stacking (Fig. 35B). This stacking propensity is similar to the PDI core-related fluorescence emission excitated at 477 nm (Fig. 35C).

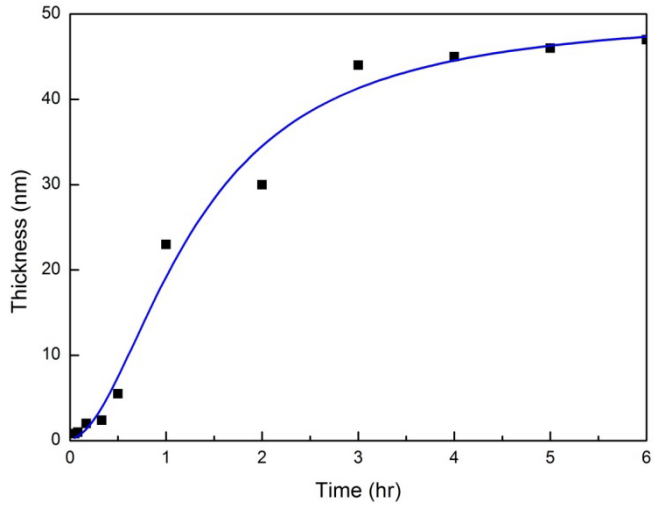

Figure 34. Thickness change of crosslinked Y-PDI film depending on UV irradiation time.

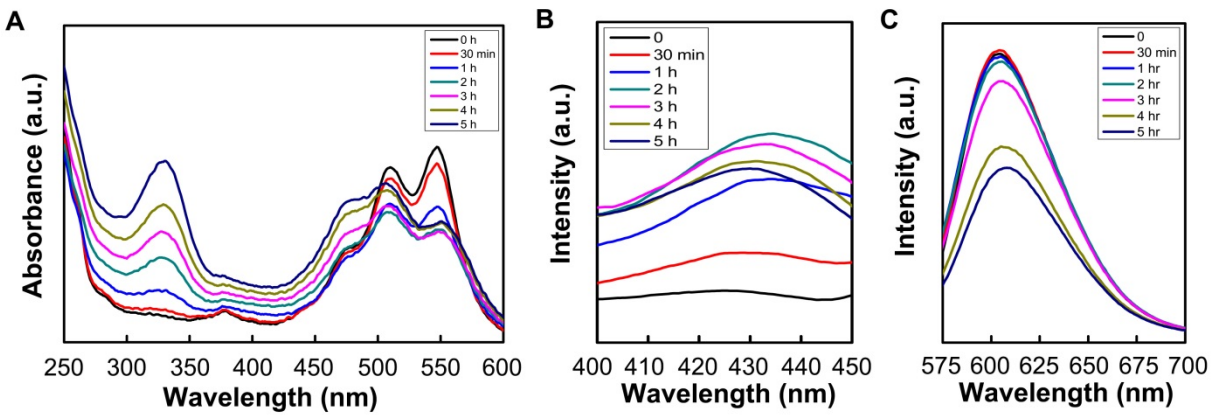

Figure 35. UV irradiation time-dependent UV-vis and fluorescence emission spectra of Y-PDI in 0.1 M CAPS buffer solution (pH 10). (A) UV/Vis absorption spectra of Y-PDI depending on UV-irradiation time. (B-C) Fluorescence emission spectra of Y-PDI depending on UV-irradiation time under 330 nm excitation (B) and 477 nm excitation (C).

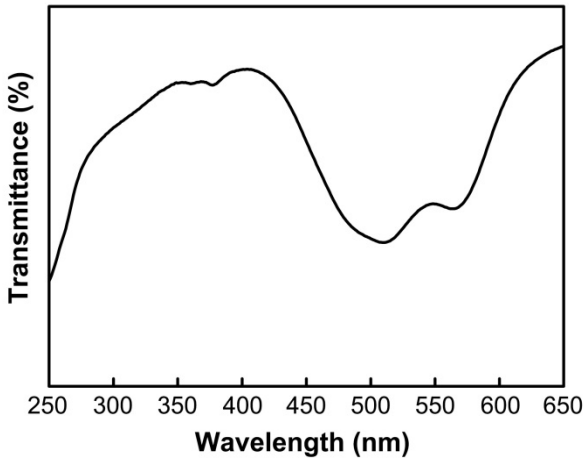

Figure 36. UV-vis spectrum of crosslinked Y-PDI film.

The UV irradiation time-dependent diTyr crosslinking of the Y-PDI was analyzed by ^{1}H nuclear magentic resonance (NMR) spectroscopy. Upon increasing UV irradiation time, the signals of the tyrosine's phenol ring were changed (Fig. 37), and new peaks appeared in the phenol ring region (6.5 ~ 7.1 ppm), indicating that the crosslinking occured between the ortho-positions of the phenol rings by diradical reaction.[169,170] In addition, the entire peaks were broadened and up-shifted due to the different levels of the pi electron delocalization of the di-tyrosine or tyrosine moieties. To corroborate the pi-pi stacking between the perylene cores, rotating-frame nuclear Overhauser effect (ROESY) NMR experiments were performed (Fig. 38). If the protons of the dityrosines and the perylene cores are in close vicinity, cross-coupling peaks would be observed. However, the cross-coupling peak can not be seen. Therefore, the possibility of the stackings between PDI cores is very high.

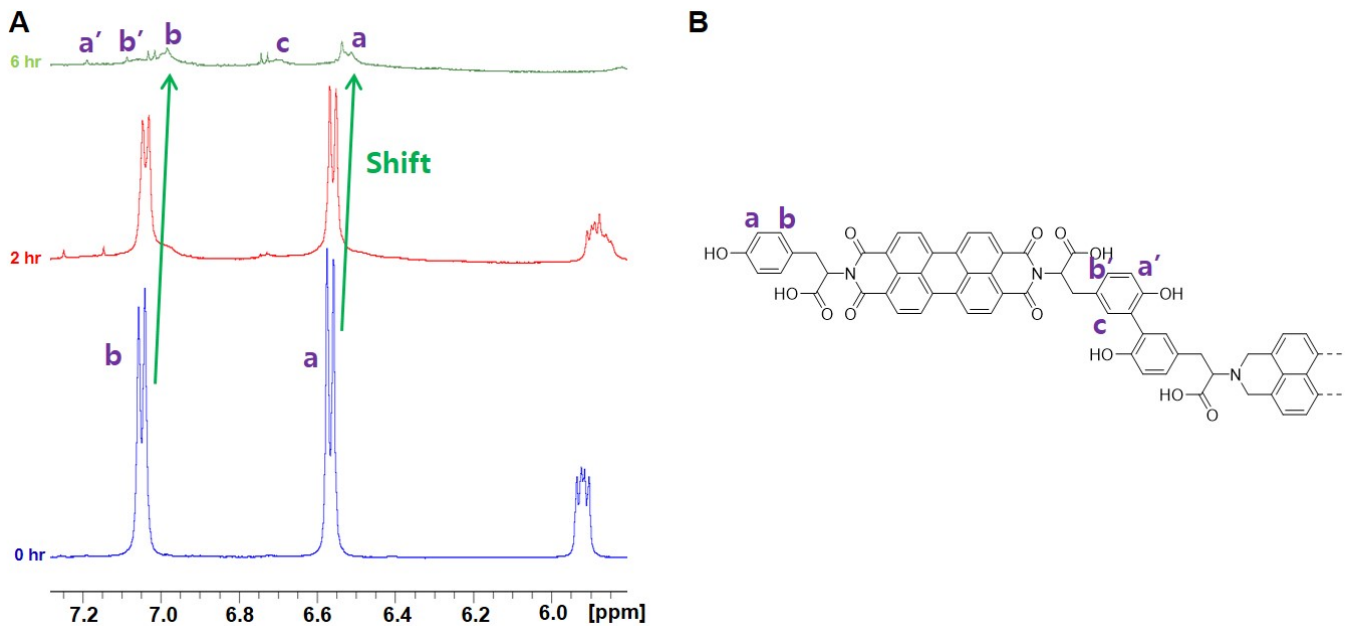

Figure 37. (A) UV irradiation time-dependent ^{1}H-NMR spectra and (B) assignment of Y-PDI in DMSO at 298 K showing the phenolic region of the tyrosines.

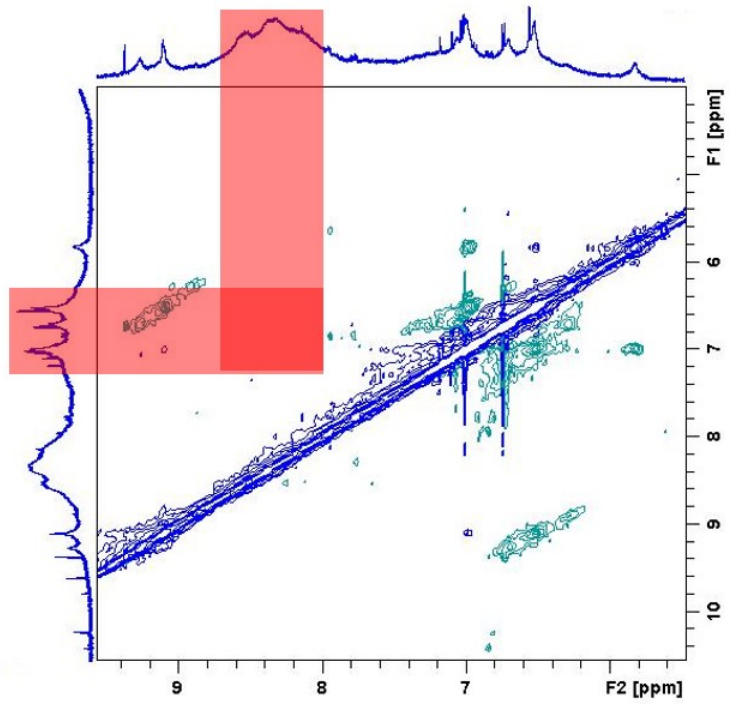

Figure 38. Representative 2D 1H/1H chemical shift correlation NMR ROESY spectrum of Y-PDI photo-crosslinked during 6 hr of UV irradiation.

The detailed structure of the crosslinked Y-PDI film was determined by high resolution TEM (HR-TEM; Fig. 39B) and powder X-ray diffraction (XRD; Fig. 39A). According to XRD, many peaks, which are usually observed in metals or well-packed organic molecules, are shown in the crosslinked Y-PDI films. The crystallinity is an important factor for organic semiconducting polymers, which is directly related to the electron and hole mobilities. In addition, HR-TEM of the polymeric film partly revealed the electron diffraction pattern of the structural ordering and crystallinity. The HR-TEM shows that the measured inter-distances between the crosslinked Y-PDI chains are 3.6 Å and 4.3 Å, which matches well with the observed d spacing from XRD data. The 3.6 Å peak is corresponding to pi stacking of the PDI cores.[171,172] The 8.3 Å (from XRD data) and 4.3 Å spacing is due to the edge-to-edge (center-to-center) ordering of the PDI cores, which is closely correlated to the arrangement of the moiety at the PDI's imide position.[171,173]

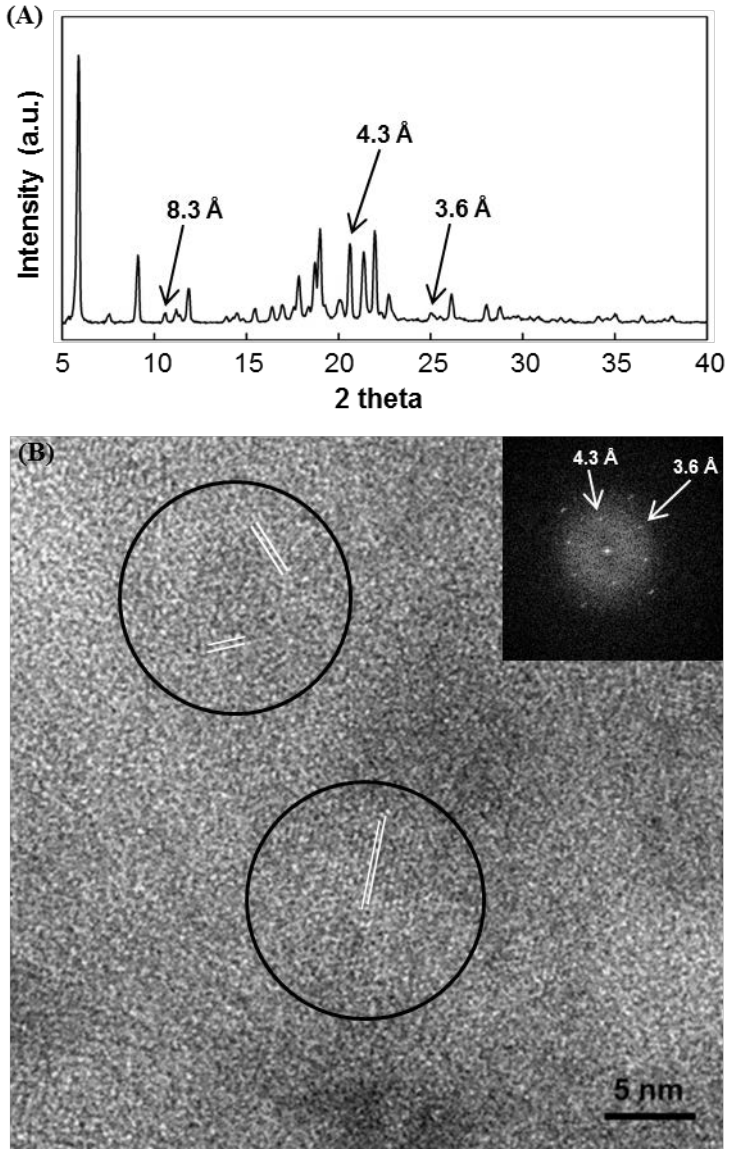

Figure 39. Structural analysis of the crosslinked Y-PDI film. (A) powder XRD of the crosslinked Y-PDI film. (B) HR-TEM image and selected area electron diffraction (SAED) pattern of the crosslinked Y-PDI film.

3.3. Molecular Mechansim for the Formation of Self-floating Crosslinked PDI Film

Self-floating phenomenon has been shown in the case of self-assembly of amphiphilic molecules. Peptides having repetitive hydrophilic and hydrophobic amino acid residues (Pro-Glu-(Phe-Glu)$_n$-Pro[174] and peptide BS30G[42]) assembled into highly ordered beta strand and film at the air/water interface. In addition, anthracene-containing amphipilic molecules were organized into monolayer sheet and polymerized at the air-water interface.[175-177] In our case, the crosslinked Y-PDI is an amphiphilic molecule at pH 10, which contains hydrophobic PDIs and hydrophilic carboxylate anions of the Tyrs. To prove the contribution of the amphiphilic structure to the self-floating, the surface activity of UV-irradiated Y-PDI was characterized by the Wilhelmy plate mothod. The time-dependent surface pressure change of the Y-PDI solution during the assembly of UV-irradiated Y-PDI was monitored at various concentration. During UV-irradiation, the surface pressure of the Y-PDI solution increased rapidly at the

beginning and then reached to the maximum value, followed by slightly decreasing. This trend was slightly different from the typical pattern of amphiphilic molecules at the air/water interface which generally exhibited the saturation curve. The higher the concentration, the larger the maximum pressure attained. This type of behavior is in good agreement with the adsorption amount of the crosslinked Y-PDI affecting the thickness of the film (Fig. 40). Based on the molecular and experimental results, the mechanism of the self-floating phenomenon can be proposed. The Y-PDIs are deprotonated and solubilized in pH 10, and gradually polymerized by UV light. The amphiphilic crosslinked Y-PDIs adsorb on the air/water interface, and the pi-pi interactions among the PDIs induced self-organization. The seed of the crosslinked Y-PDI assembly at the interface laterally grow to cover the overall surface.

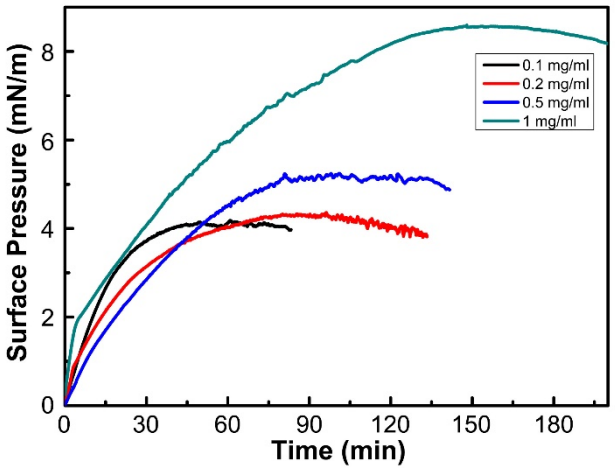

Figure 40. Surface pressure-UV irradiation time isotherms for the crosslinked Y-PDI film formation at different concentrations (0.1, 0.2, 0.5, 1.0 mg/ml).

3.4. Evaluation of Crosslinked Y-PDI film as Photocurrent Generator

The pi-electron delocalization through the 2D arrangement of PDI is expected to give charge transport pathway. As shown in Figure 41, the crosslinked Y-PDI films hardly afforded conductive property in dark condition. When irradiated with white light, the I-V curves of the film showed good ohmic behavior of the electrical conduction. As shown as Figure 42, the photocurrent had the linear dependence of the light intensity measured at an applied bias of 3 V, which indicates that the charge carrier photogeneration is proportional to the absorbed photon flux.[178] This photocurrent can be generated by the PDI radical anion ($PDI^{\bullet -}$). Previously, the amino acid-appended PDIs aqueous solutions were dropcasted onto substrate for film formation. [179,180] With this dropcasting method, it is difficult to control the thickness of the films and analyze the accurate device performance. In this context, the thickness controllable film fabrication method using UV irradiation has an advantage. In

addition, the repeatable photocurrent switching could be obtained by turning the white light (4.42 mW/cm^2) on and off (Fig. 43) with 3 V applied bias. Expectedly, the off-current didn't completely return to the initial current and the entire current gradually increased. It can be explained that the trapped electrons in the defect site inside the film slowly flows into electrode when light was off. [181] Figure 44 shows the photocurrent propensity depending on different wavelength (365 nm, 550 nm, and 900 nm). We expected that 550 nm of visible light, which belongs to the main absorbtion range of the PDI, can drive the highest current.[182] However, irradiation with 365 nm (UV range) gave the highest photocurrent, which could be induced by radical anion and dianion formed by UV [180]. Additionally, we found out that the increase of the base current shown in Figure 43 was due to radical anion and dianion by UV light.

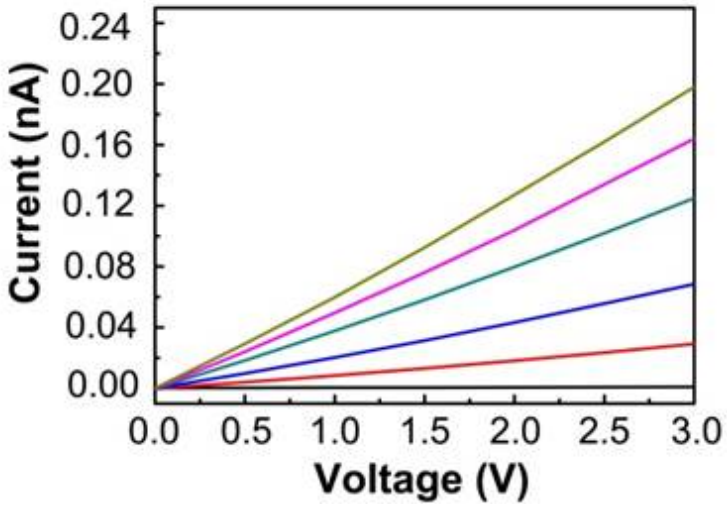

Figure 41. Current-voltage curves measured over the crosslinked PDI-Y films in the dark (black) and under white light irradiation of increasing power density (red: 50 cd, blue: 100 cd, cyan: 150 cd, pink: 200 cd, gold: 250 cd) in vacuum.

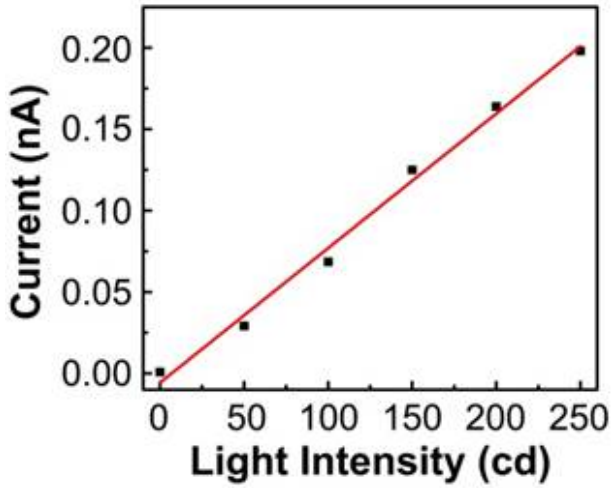

Figure 42. Photocurrent of the crosslinked PDI-Y film measured as a function of white light intensity with 3 V applied bias.

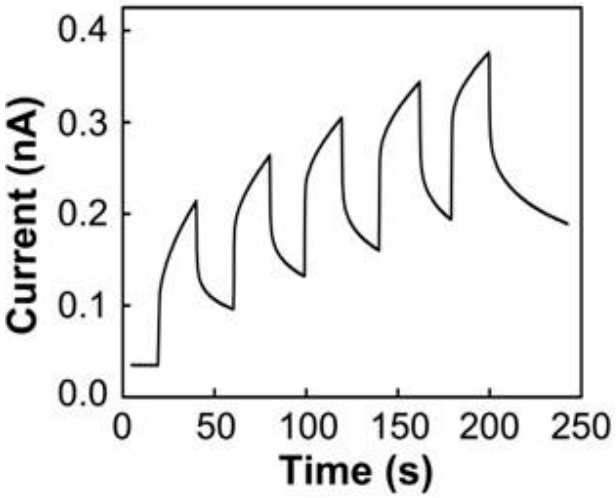

Figure 43. Photocurrent (at 3 V) in response to turning on and off the irradiation (250 cd, 4.42 mW/cm^2).

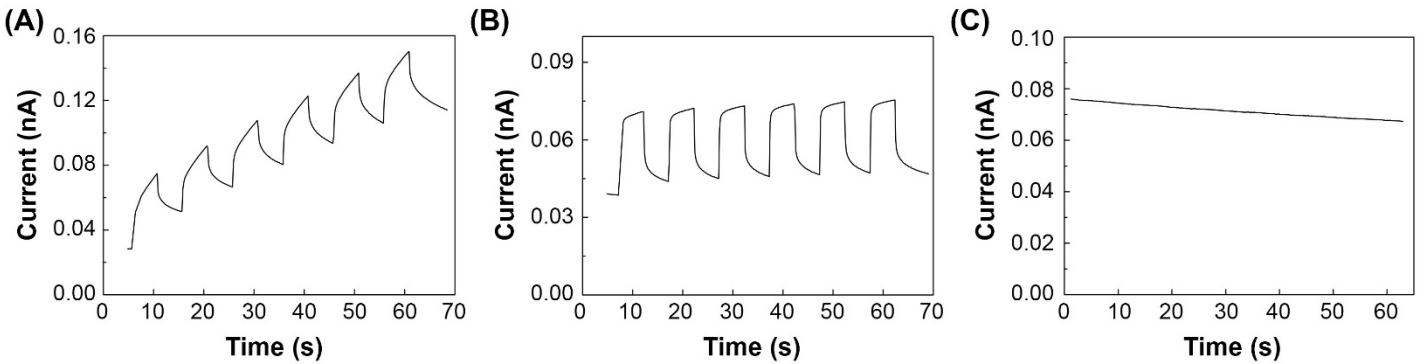

Figure 44. Photocurrent switching behavior under different wavelength illumination ((A) UV region (365 nm, 115 μW/cm^2), (B) visible region (550 nm, 1.31 mW/cm^2), (C) NIR region (900 nm, 242 μW/cm^2)).

In terms of light harvesting, the charge separation and charge recombination are important factors. To further investigate the photoresponse of the crosslinked Y-PDI film, femtosecond transient absorption (fs-TA) studies were performed at room temperature on Y-PDI and crosslinked Y-PDI in 0.1 M CAPS buffer (pH 10). As shown in Figure 45A, the fs-TA spectrum of the Y-PDI shows broad positive feature in near-IR region (around 730 nm) corresponding to typical $PDI^{\bullet -}$ peak.[183-185] This phenomenon appears in the case of the crosslinked Y-PDI, but the disturbance of light penetration, induced by its stacking, produces low intensity compared to the Y-PDI. In the crosslinked Y-PDI, decay kinetics at 730 nm was 2.3 ps, which is factor than that of Y-PDI 3.9 ps during the early stage of time profile, as shown as Figure 45B. This result might come from a rapid charge separation by the tight stacking of the crosslinked Y-PDI. As the time elapses, slower decay region with 254 ps appears due to its electron transport along the pi-stacked PDIs. This charge recombination time is similar to the previous study.[186] This slow charge recombination is due to the relaxation from long-lived

charge separated (crosslinked Y-PDI)$_n$•$^-$. Therefore, the photocurrent generation property of the crosslinked PDI-Y film can be explained by the charge-delocalized state with a longer lifetime.

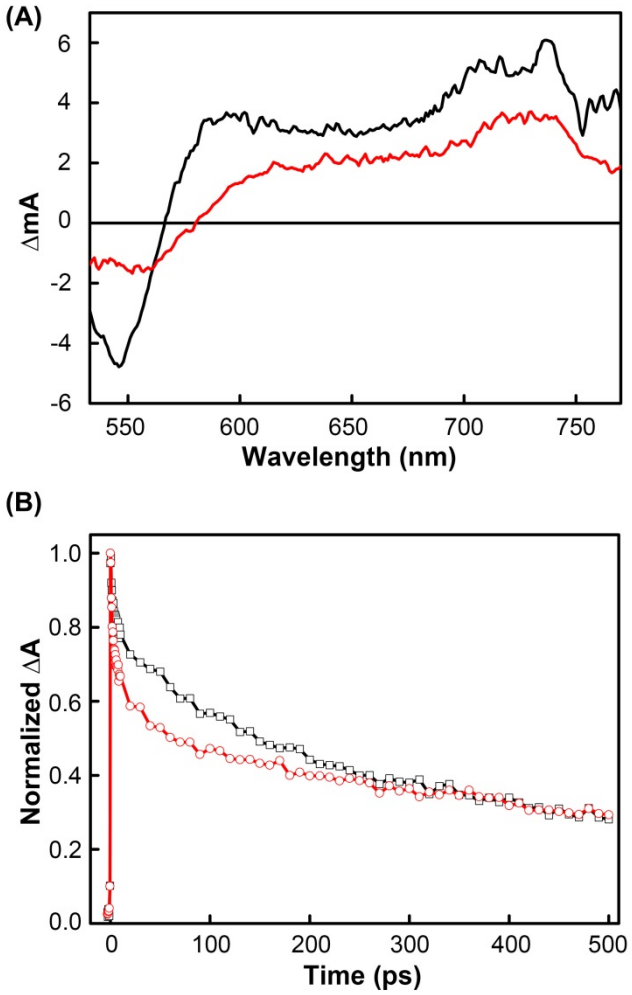

Figure 45. Transient absorption spectra for Y-PDI monomer (black) and crosslinked Y-PDI (red). (A) Transient absorption spectra at 1 ps after the pulse excitation. (B) Time profiles monitored at 730 nm.

3.5. Effect of Spacer Amino Acid between Tyrosine and PDI to Photocurrent Generation

To control stacking of the PDI core, glycine (Gly, G) as a flexible space was introduced between tyrosine and PDI. The resulting YG-PDI was dissolved in 0.1 M CAPS buffer (pH 10) in the same way as the Y-PDI, and assembled into a film. The crosslinked YG-PDI film was transferred into the interdigitized electrode. As shown in Figure 46, the I-V curves of the crosslinked YG-PDI films represented similar propensity, but the entire photocurrent was higher than that of the Y-PDI film. The photocurrent (3.1 nA) of the YG-PDI film under white light illumination at an applied bias of 3 V was dramatically increased by ca. 15 times compared with that (0.2 nA) of the Y-PDI film (Fig. 47). This result could be interpretated by the UV spectra of the crosslinked YG-PDI (Fig. 48). Compared with the UV spectra of the Y-PDI (Fig. 34A), the crosslinked YG-PDI gave broadened and red shifted UV-Vis absorption bands, which is due to the pi-electron delocalization between the pi-stacked PDI.[187]

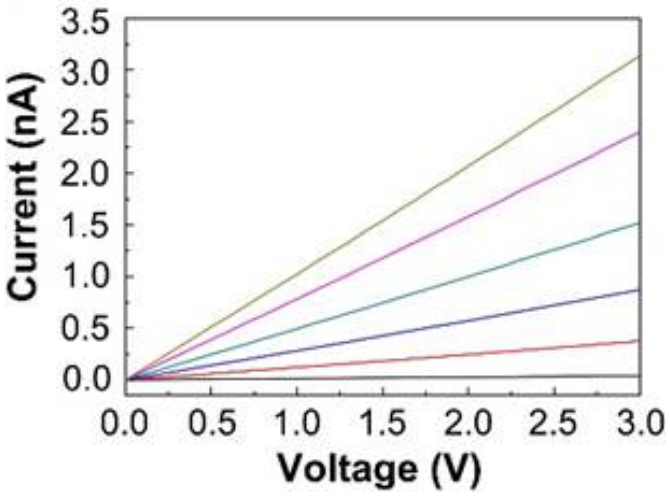

Figure 46. Current-voltage curves measured over the crosslinked GY-PDI films in the dark (black) and under white light irradiation of increasing power density (red: 50 cd, blue: 100 cd, cyan: 150 cd, pink: 200 cd, gold: 250 cd) in vacuum.

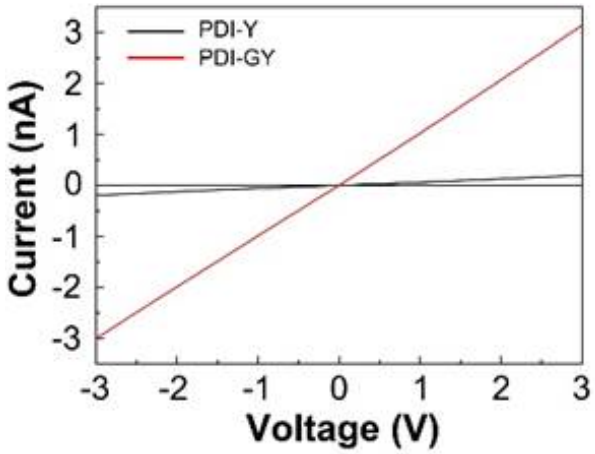

Figure 47. Current-voltage curves for the crosslinked Y-PDI film (black) and the crosslinked YG-PDI film (red) under white light irradiation with a power density of 250 cd.

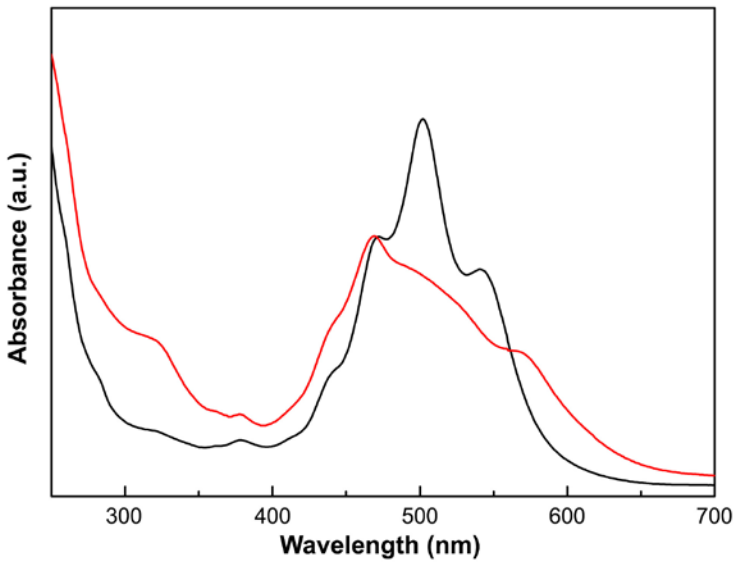

Figure 48. UV-vis spectra before (black) and after (red) UV-induced crosslinking of YG-PDI.

4. Conclusion

We have demonstrated a possibility of using dityrosine crosslinking to assemble PDI cores into semi-crystalline 2D film at the air/water interface for photocurrent generation. The formation of the dityrosine crosslinking induced the pi-pi stacking of the PDI cores and the resulting amphiphilic property of the crosslinked Y-PDI molecules made the films float at air/water interface. The thickness of the crosslinked Y-PDI films was controlled by the amount of the dityrosine crosslinkages with increasing UV-irradiation time. Due to the stacked PDI cores, the crosslinked Y-PDI films were reactive for whitelight. The flexible amino acid spacer, Gly, located between the tyrosine and the PDI core increased pi-electron delocalization of the PDI, resulting in more efficient photocurrent generation.

References

1. Kotov, N. Layer-by-layer self-assembly: the contribution of hydrophobic interactions. *Nanostructured Materials* **12**, 789-796 (1999).
2. Meyer, E. E., Rosenberg, K. J. & Israelachvili, J. Recent progress in understanding hydrophobic interactions. *Proceedings of the National Academy of Sciences* **103**, 15739-15746 (2006).
3. Chen, Q., Bae, S. C. & Granick, S. Directed self-assembly of a colloidal kagome lattice. *Nature* **469**, 381-384 (2011).
4. Hirschberg, J. K. *et al.* Helical self-assembled polymers from cooperative stacking of hydrogen-bonded pairs. *Nature* **407**, 167-170 (2000).
5. Davis, J. T. & Spada, G. P. Supramolecular architectures generated by self-assembly of guanosine derivatives. *Chemical Society Reviews* **36**, 296-313 (2007).
6. Chen, K. M., Jiang, X., Kimerling, L. C. & Hammond, P.

T. Selective self-organization of colloids on patterned polyelectrolyte templates. *Langmuir* **16**, 7825-7834 (2000).

7. Kötz, J., Kosmella, S. & Beitz, T. Self-assembled polyelectrolyte systems. *Progress in Polymer Science* **26**, 1199-1232 (2001).

8. Northrop, B. H., Zheng, Y.-R., Chi, K.-W. & Stang, P. J. Self-organization in coordination-driven self-assembly. *Accounts of Chemical Research* **42**, 1554-1563 (2009).

9. Ahrens, M. J. *et al.* Self-assembly of supramolecular light-harvesting arrays from covalent multi-chromophore perylene-3, 4: 9, 10-bis (dicarboximide) building blocks. *Journal of the American Chemical Society* **126**, 8284-8294 (2004).

10. Ryu, J.-H., Hong, D.-J. & Lee, M. Aqueous self-assembly of aromatic rod building blocks. *Chemical Communications*, 1043-1054 (2008).

11. Guo, Y. *et al.* Self-Assembly of functional molecules into 1D crystalline nanostructures. *Advanced Materials*

27, 985-1013 (2015).

12. Shen, C.-L. & Murphy, R. M. Solvent effects on self-assembly of beta-amyloid peptide. *Biophysical Journal* **69**, 640 (1995).

13. Cui, H., Chen, Z., Zhong, S., Wooley, K. L. & Pochan, D. J. Block copolymer assembly via kinetic control. *Science* **317**, 647-650 (2007).

14. Xu, J. *et al.* Asymmetric and symmetric dipole−dipole interactions drive distinct aggregation and emission behavior of intramolecular charge-transfer molecules. *The Journal of Physical Chemistry C* **113**, 5924-5932 (2009).

15. Gummel, J., Sztucki, M., Narayanan, T. & Gradzielski, M. Concentration dependent pathways in spontaneous self-assembly of unilamellar vesicles. *Soft Matter* **7**, 5731-5738 (2011).

16. Bong, D. T., Clark, T. D., Granja, J. R. & Ghadiri, M. R. Self-assembling organic nanotubes. *Angewandte Chemie International Edition* **40**, 988-1011 (2001).

17. Zhang, S. Fabrication of novel biomaterials through molecular self-assembly. *Nature Biotechnology* **21**, 1171-1178 (2003).

18. Sarikaya, M., Tamerler, C., Jen, A. K.-Y., Schulten, K. & Baneyx, F. Molecular biomimetics: nanotechnology through biology. *Nature materials* **2**, 577-585 (2003).

19. Barnes, C. P., Sell, S. A., Boland, E. D., Simpson, D. G. & Bowlin, G. L. Nanofiber technology: designing the next generation of tissue engineering scaffolds. *Advanced Drug Delivery Reviews* **59**, 1413-1433 (2007).

20. Gazit, E. Self-assembled peptide nanostructures: the design of molecular building blocks and their technological utilization. *Chemical Society Reviews* **36**, 1263-1269 (2007).

21. Ulijn, R. V. & Smith, A. M. Designing peptide based nanomaterials. *Chemical Society Reviews* **37**, 664-675 (2008).

22. Cui, H., Webber, M. J. & Stupp, S. I. Self-assembly of peptide amphiphiles: From molecules to nanostructures

to biomaterials. *Peptide Science* **94**, 1-18 (2010).

23. Ghadiri, M. R., Granja, J. R., Milligan, R. A., McRee, D. E. & Khazanovich, N. Self-assembling organic nanotubes based on a cyclic peptide architecture. *Nature* **366**, 324-327 (1993).

24. Reches, M. & Gazit, E. Casting metal nanowires within discrete self-assembled peptide nanotubes. *Science* **300**, 625-627 (2003).

25. Scherzinger, E. *et al.* Self-assembly of polyglutamine-containing huntingtin fragments into amyloid-like fibrils: implications for Huntington's disease pathology. *Proceedings of the National Academy of Sciences* **96**, 4604-4609 (1999).

26. Thirumalai, D., Klimov, D. & Dima, R. Emerging ideas on the molecular basis of protein and peptide aggregation. *Current Opinion in Structural Biology* **13**, 146-159 (2003).

27. Wu, C., Lei, H. & Duan, Y. Formation of partially ordered oligomers of amyloidogenic hexapeptide

(NFGAIL) in aqueous solution observed in molecular dynamics simulations. *Biophysical Journal* **87**, 3000-3009 (2004).

28. Easterhoff, D., DiMaio, J. T., Doran, T. M., Dewhurst, S. & Nilsson, B. L. Enhancement of HIV-1 infectivity by simple, self-assembling modular peptides. *Biophysical Journal* **100**, 1325-1334 (2011).

29. Matos, C. A., de Macedo-Ribeiro, S. & Carvalho, A. L. Polyglutamine diseases: the special case of ataxin-3 and Machado–Joseph disease. *Progress in Neurobiology* **95**, 26-48 (2011).

30. Hauser, C. A. *et al.* Natural tri-to hexapeptides self-assemble in water to amyloid β-type fiber aggregates by unexpected α-helical intermediate structures. *Proceedings of the National Academy of Sciences* **108**, 1361-1366 (2011).

31. Jayawarna, V., Smith, A., Gough, J. & Ulijn, R. Three-dimensional cell culture of chondrocytes on modified di-phenylalanine scaffolds. *Biochemical Society*

Transactions **35**, 535-537 (2007).

32. Tang, C., Smith, A. M., Collins, R. F., Ulijn, R. V. & Saiani, A. Fmoc-diphenylalanine self-assembly mechanism induces apparent p K a shifts. *Langmuir* **25**, 9447-9453 (2009).

33. Zhou, M. *et al.* Self-assembled peptide-based hydrogels as scaffolds for anchorage-dependent cells. *Biomaterials* **30**, 2523-2530 (2009).

34. Bai, S. *et al.* Stable emulsions formed by self-assembly of interfacial networks of dipeptide derivatives. *ACS nano* **8**, 7005-7013 (2014).

35. Ghadiri, M. R., Granja, J. R. & Buehler, L. Artificial transmembrane ion channels from self-assembling. *Nature* **369**, 301-304 (1994).

36. Görbitz, C. H. Nanotube formation by hydrophobic dipeptides. *Chemistry–A European Journal* **7**, 5153-5159 (2001).

37. Vauthey, S., Santoso, S., Gong, H., Watson, N. & Zhang, S. Molecular self-assembly of surfactant-like peptides to

form nanotubes and nanovesicles. *Proceedings of the National Academy of Sciences* **99**, 5355-5360 (2002).

38. Morikawa, M. a., Yoshihara, M., Endo, T. & Kimizuka, N. α-Helical polypeptide microcapsules formed by emulsion-templated self-Assembly. *Chemistry–A European Journal* **11**, 1574-1578 (2005).

39. Yan, X., Zhu, P., Fei, J. & Li, J. Self-assembly of peptide-inorganic hybrid spheres for adaptive encapsulation of guests. *Advanced Materials* **22**, 1283-1287 (2010).

40. Fletcher, J. M. *et al.* Self-assembling cages from coiled-coil peptide modules. *Science* **340**, 595-599 (2013).

41. Zhang, S., Holmes, T., Lockshin, C. & Rich, A. Spontaneous assembly of a self-complementary oligopeptide to form a stable macroscopic membrane. *Proceedings of the National Academy of Sciences* **90**, 3334-3338 (1993).

42. Rapaport, H. *et al.* Assembly of triple-stranded β-sheet peptides at interfaces. *Journal of the American Chemical*

Society **124**, 9342-9343 (2002).

43. Jang, H.-S. *et al.* Tyrosine-mediated two-dimensional peptide assembly and its role as a bio-inspired catalytic scaffold. *Nature communications* **5** (2014).

44. Wang, D. *et al.* 2D protein supramolecular nanofilm with exceptionally large area and emergent functions. *Advanced Materials* **28**, 7414-7423 (2016).

45. Kisiday, J. *et al.* Self-assembling peptide hydrogel fosters chondrocyte extracellular matrix production and cell division: implications for cartilage tissue repair. *Proceedings of the National Academy of Sciences* **99**, 9996-10001 (2002).

46. Ruan, L. *et al.* Designed amphiphilic peptide forms stable nanoweb, slowly releases encapsulated hydrophobic drug, and accelerates animal hemostasis. *Proceedings of the National Academy of Sciences* **106**, 5105-5110 (2009).

47. Inostroza-Brito, K. E. *et al.* Co-assembly, spatiotemporal control and morphogenesis of a hybrid protein–peptide

system. *Nature chemistry* **7**, 897-904 (2015).

48. Kim, S., Kim, J. H., Lee, J. S. & Park, C. B. Beta-Sheet-Forming, Self-assembled peptide nanomaterials towards optical, energy, and healthcare applications. *Small* **11**, 3623-3640 (2015).

49. Hartgerink, J. D., Beniash, E. & Stupp, S. I. Self-assembly and mineralization of peptide-amphiphile nanofibers. *Science* **294**, 1684-1688 (2001).

50. Silva, G. A. *et al.* Selective differentiation of neural progenitor cells by high-epitope density nanofibers. *Science* **303**, 1352-1355 (2004).

51. Israelachvili, J. N. *Intermolecular and Surface Forces*. (Academic Press, 1992).

52. Palmer, L. C. & Stupp, S. I. Molecular self-assembly into one-dimensional nanostructures. *Accounts of Chemical Research* **41**, 1674-1684 (2008).

53. Niece, K. L., Hartgerink, J. D., Donners, J. J. & Stupp, S. I. Self-assembly combining two bioactive peptide-amphiphile molecules into nanofibers by electrostatic

attraction. *Journal of the American Chemical Society* **125**, 7146-7147 (2003).

54. Yuwono, V. M. & Hartgerink, J. D. Peptide amphiphile nanofibers template and catalyze silica nanotube formation. *Langmuir* **23**, 5033-5038 (2007).

55. Pierschbacher, M. D. & Ruoslahti, E. Cell attachment activity of fibronectin can be duplicated by small synthetic fragments of the molecule. *Nature* **309**, 30 (1984).

56. Pierschbacher, M. D. & Ruoslahti, E. Variants of the cell recognition site of fibronectin that retain attachment-promoting activity. *Proceedings of the National Academy of Sciences* **81**, 5985-5988 (1984).

57. Storrie, H. *et al.* Supramolecular crafting of cell adhesion. *Biomaterials* **28**, 4608-4618 (2007).

58. Woolfson, D. N. & Ryadnov, M. G. Peptide-based fibrous biomaterials: some things old, new and borrowed. *Current Opinion in Chemical Biology* **10**, 559-567 (2006).

59. Cinar, G. *et al.* Amyloid inspired self-assembled peptide nanofibers. *Biomacromolecules* **13**, 3377-3387 (2012).

60. Marullo, R., Kastantin, M., Drews, L. B. & Tirrell, M. Peptide contour length determines equilibrium secondary structure in protein-analogous micelles. *Biopolymers* **99**, 573-581 (2013).

61. Frederix, P. W. *et al.* Exploring the sequence space for (tri-) peptide self-assembly to design and discover new hydrogels. *Nature chemistry* **7**, 30-37 (2015).

62. Pietropaolo, A. *et al.* Unveiling the role of histidine and tyrosine residues on the conformation of the avian prion hexarepeat domain. *The Journal of Physical Chemistry B* **112**, 5182-5188 (2008).

63. Minor Jr, D. L. & Kimf, P. S. ß-sheet-forming propensities of amino acids. *Nature* **367**, 17 (1994).

64. Smith, C. K., Withka, J. M. & Regan, L. A Thermodynamic scale for the beta-sheet forming tendencies of the amino acids. *Biochemistry* **33**, 5510-5517 (1994).

65. Biancalana, M., Makabe, K., Koide, A. & Koide, S. Aromatic cross-strand ladders control the structure and stability of β-rich peptide self-assembly mimics. *Journal of Molecular Biology* **383**, 205-213 (2008).

66. Richardson, J. S. beta-sheet topology and the relatedness of proteins. *Nature* **268**, 495-500 (1977).

67. Hemmingsen, J. M., Gernert, K. M., Richardson, J. S. & Richardson, D. C. The tyrosine corner: a feature of most Greek key β-barrel proteins. *Protein Science* **3**, 1927-1937 (1994).

68. Bagby, S., Go, S., Inouye, S., Ikura, M. & Chakrabartty, A. Equilibrium folding intermediates of a Greek key β-barrel protein. *Journal of Molecular Biology* **276**, 669-681 (1998).

69. Hamill, S. J., Cota, E., Chothia, C. & Clarke, J. Conservation of folding and stability within a protein family: the tyrosine corner as an evolutionary cul-de-sac. *Journal of Molecular Biology* **295**, 641-649 (2000).

70. Marazzi, M., Navizet, I., Lindh, R. & Frutos, L. M.

Photostability mechanisms in human γB-crystallin: Role of the tyrosine corner unveiled by quantum mechanics and hybrid quantum mechanics/molecular mechanics methodologies. *Journal of chemical theory and computation* **8**, 1351-1359 (2012).

71. Hammarström, L. & Styring, S. Proton-coupled electron transfer of tyrosines in Photosystem II and model systems for artificial photosynthesis: the role of a redox-active link between catalyst and photosensitizer. *Energy & Environmental Science* **4**, 2379-2388 (2011).

72. Reece, S. Y., Seyedsayamdost, M. R., Stubbe, J. & Nocera, D. G. Direct observation of a transient tyrosine radical competent for initiating turnover in a photochemical ribonucleotide reductase. *Journal of the American Chemical Society* **129**, 13828-13830 (2007).

73. Reguera, G. *et al.* Extracellular electron transfer via microbial nanowires. *Nature* **435**, 1098-1101 (2005).

74. Malvankar, N. S. *et al.* Tunable metallic-like conductivity in microbial nanowire networks. *nature*

nanotechnology **6**, 573-579 (2011).

75. Bonanni, P. S., Massazza, D. & Busalmen, J. P. Stepping stones in the electron transport from cells to electrodes in Geobacter sulfurreducens biofilms. *Physical Chemistry Chemical Physics* **15**, 10300-10306 (2013).

76. Pagba, C. V., Chi, S.-H., Perry, J. & Barry, B. A. Proton-coupled electron transfer in tyrosine and a β-hairpin maquette: Reaction dynamics on the picosecond time scale. *The Journal of Physical Chemistry B* **119**, 2726-2736 (2014).

77. Pagba, C. V. *et al.* A tyrosine-tryptophan dyad and radical-based charge transfer in a ribonucleotide reductase-inspired maquette. *Nature communications* **6** (2015).

78. Pagba, C. V., McCaslin, T. G., Chi, S.-H., Perry, J. W. & Barry, B. A. Proton-coupled electron transfer and a tyrosine–histidine pair in a photosystem II-inspired β-hairpin maquette: Kinetics on the picosecond time scale. *The Journal of Physical Chemistry B* **120**, 1259-1272

(2016).

79. Sjödin, M. *et al.* Switching the redox mechanism: models for proton-coupled electron transfer from tyrosine and tryptophan. *Journal of the American Chemical Society* **127**, 3855-3863 (2005).

80. Irebo, T., Reece, S. Y., Sjödin, M., Nocera, D. G. & Hammarström, L. Proton-coupled electron transfer of tyrosine oxidation: Buffer dependence and parallel mechanisms. *Journal of the American Chemical Society* **129**, 15462-15464 (2007).

81. Zhang, M.-T. & Hammarström, L. Proton-coupled electron transfer from tryptophan: A concerted mechanism with water as proton acceptor. *Journal of the American Chemical Society* **133**, 8806-8809 (2011).

82. Stadtman, E. Oxidation of free amino acids and amino acid residues in proteins by radiolysis and by metal-catalyzed reactions. *Annual Review of Biochemistry* **62**, 797-821 (1993).

83. Lehrer, S. & Fasman, G. D. Ultraviolet irradiation

effects in poly-L-tyrosine and model compounds. identification of bityrosine as a photoproduct*. *Biochemistry* **6**, 757-767 (1967).

84. Holler, T. P. & Hopkins, P. B. A qualitative fluorescence-based assay for tyrosyl radical scavenging activity: ovothiol A is an efficient scavenger. *Analytical Biochemistry* **180**, 326-330 (1989).

85. Yoburn, J. C. *et al.* Dityrosine cross-linked Aβ peptides: Fibrillar β-structure in Aβ (1-40) is conducive to formation of dityrosine cross-links but a dityrosine cross-link in Aβ (8-14) does not induce β-structure. *Chemical Research in Toxicology* **16**, 531-535 (2003).

86. Brown, K. C., Yang, S.-H. & Kodadek, T. Highly specific oxidative crosslinking of proteins mediated by a nickel-peptide complex. *Biochemistry* **34**, 4733-4739 (1995).

87. Atwood, C. S. *et al.* Copper mediates dityrosine cross-linking of Alzheimer's amyloid-β. *Biochemistry* **43**, 560-568 (2004).

88. MacGregor, H. J., Kato, Y., Marshall, L. J., Nevell, T. G. & Shute, J. K. A copper–hydrogen peroxide redox system induces dityrosine cross-links and chemokine oligomerisation. *Cytokine* **56**, 669-675 (2011).

89. Fancy, D. A. & Kodadek, T. Chemistry for the analysis of protein–protein interactions: rapid and efficient cross-linking triggered by long wavelength light. *Proceedings of the National Academy of Sciences* **96**, 6020-6024 (1999).

90. Elvin, C. M. *et al.* Synthesis and properties of crosslinked recombinant pro-resilin. *Nature* **437**, 999-1002 (2005).

91. Truong, M. Y. *et al.* The effect of hydration on molecular chain mobility and the viscoelastic behavior of resilin-mimetic protein-based hydrogels. *Biomaterials* **32**, 8462-8473 (2011).

92. Ding, Y., Li, Y., Qin, M., Cao, Y. & Wang, W. Photo-cross-linking approach to engineering small Tyrosine-containing peptide hydrogels with enhanced mechanical

stability. *Langmuir* **29**, 13299-13306 (2013).

93. Ding, D. *et al.* From soft self-healing gels to stiff films in suckerin-based materials through modulation of crosslink density and β-sheet content. *Advanced Materials* **27**, 3953-3961 (2015).

94. Giulivi, C., Traaseth, N. & Davies, K. Tyrosine oxidation products: analysis and biological relevance. *Amino Acids* **25**, 227-232 (2003).

95. Weis-Fogh, T. Molecular interpretation of the elasticity of resilin, a rubber-like protein. *Journal of Molecular Biology* **3**, 648-667 (1961).

96. Lv, S. *et al.* Designed biomaterials to mimic the mechanical properties of muscles. *Nature* **465**, 69-73 (2010).

97. Young, D. & Bennet-Clark, H. The role of the tymbal in cicada sound production. *Journal of Experimental Biology* **198**, 1001-1020 (1995).

98. Kurisawa, M., Chung, J. E., Yang, Y. Y., Gao, S. J. & Uyama, H. Injectable biodegradable hydrogels

composed of hyaluronic acid–tyramine conjugates for drug delivery and tissue engineering. *Chemical Communications*, 4312-4314 (2005).

99. Jin, R., Hiemstra, C., Zhong, Z. & Feijen, J. Enzyme-mediated fast in situ formation of hydrogels from dextran–tyramine conjugates. *Biomaterials* **28**, 2791-2800 (2007).

100. Sakai, S., Hirose, K., Taguchi, K., Ogushi, Y. & Kawakami, K. An injectable, in situ enzymatically gellable, gelatin derivative for drug delivery and tissue engineering. *Biomaterials* **30**, 3371-3377 (2009).

101. Liao, S. W., Yu, T.-B. & Guan, Z. De novo design of saccharide− peptide hydrogels as synthetic scaffolds for tailored cell responses. *Journal of the American Chemical Society* **131**, 17638-17646 (2009).

102. Wang, L.-S., Chung, J. E., Chan, P. P.-Y. & Kurisawa, M. Injectable biodegradable hydrogels with tunable mechanical properties for the stimulation of neurogenesic differentiation of human mesenchymal

stem cells in 3D culture. *Biomaterials* **31**, 1148-1157 (2010).

103. Wang, L.-S., Boulaire, J., Chan, P. P., Chung, J. E. & Kurisawa, M. The role of stiffness of gelatin–hydroxyphenylpropionic acid hydrogels formed by enzyme-mediated crosslinking on the differentiation of human mesenchymal stem cell. *Biomaterials* **31**, 8608-8616 (2010).

104. Park, K. M., Ko, K. S., Joung, Y. K., Shin, H. & Park, K. D. In situ cross-linkable gelatin–poly (ethylene glycol)–tyramine hydrogel via enzyme-mediated reaction for tissue regenerative medicine. *Journal of Materials Chemistry* **21**, 13180-13187 (2011).

105. Mann, S. Molecular tectonics in biomineralization and biomimetic materials chemistry. *Nature* **365**, 499-505 (1993).

106. Heywood, B. R. Synthesis of inorganic nanophase materials in supramolecular protein cages. *Nature* **349** (1991).

107. Chen, C.-L., Zhang, P. & Rosi, N. L. A new peptide-based method for the design and synthesis of nanoparticle superstructures: construction of highly ordered gold nanoparticle double helices. *Journal of the American Chemical Society* **130**, 13555-13557 (2008).

108. Su, Y. *et al.* Peptide mesocrystals as templates to create an Au surface with stronger surface-enhanced Raman spectroscopic properties. *Chemistry-A European Journal* **17**, 3370-3375 (2011).

109. Vinod, T. *et al.* Transparent, conductive, and SERS-active Au nanofiber films assembled on an amphiphilic peptide template. *Nanoscale* **5**, 10487-10493 (2013).

110. Gottlieb, D., Morin, S. A., Jin, S. & Raines, R. T. Self-assembled collagen-like peptide fibers as templates for metallic nanowires. *Journal of Materials Chemistry* **18**, 3865-3870 (2008).

111. Carter, C. J., Ackerson, C. J. & Feldheim, D. L. Unusual reactivity of a silver mineralizing peptide. *ACS nano* **4**, 3883-3888 (2010).

112. Rubio-Martínez, M., Puigmartí-Luis, J., Imaz, I., Dittrich, P. S. & Maspoch, D. “Dual-template” synthesis of one-dimensional conductive nanoparticle superstructures from coordination metal–peptide polymer crystals. *Small* **9**, 4160-4167 (2013).

113. Pacardo, D. B., Sethi, M., Jones, S. E., Naik, R. R. & Knecht, M. R. Biomimetic synthesis of Pd nanocatalysts for the Stille coupling reaction. *ACS nano* **3**, 1288-1296 (2009).

114. Jakhmola, A., Bhandari, R., Pacardo, D. B. & Knecht, M. R. Peptide template effects for the synthesis and catalytic application of Pd nanoparticle networks. *Journal of Materials Chemistry* **20**, 1522-1531 (2010).

115. Bhandari, R. & Knecht, M. R. Effects of the material structure on the catalytic activity of peptide-templated Pd nanomaterials. *Acs Catalysis* **1**, 89-98 (2011).

116. Chiu, C.-Y. *et al.* Platinum nanocrystals selectively shaped using facet-specific peptide sequences. *Nature chemistry* **3**, 393-399 (2011).

117. Ruan, L. *et al.* Tailoring molecular specificity toward a crystal facet: a lesson from biorecognition toward Pt {111}. *Nano Letters* **13**, 840-846 (2013).

118. Ruan, L. *et al.* Biomimetic synthesis of an ultrathin platinum nanowire network with a high twin density for enhanced electrocatalytic activity and durability. *Angewandte Chemie International Edition* **52**, 12577-12581 (2013).

119. Banerjee, I. A., Yu, L. & Matsui, H. Cu nanocrystal growth on peptide nanotubes by biomineralization: size control of Cu nanocrystals by tuning peptide conformation. *Proceedings of the National Academy of Sciences of the United States of America* **100**, 14678-14682 (2003).

120. Dasa, S. S. K., Jin, Q., Chen, C.-T. & Chen, L. Target-specific copper hybrid T7 phage particles. *Langmuir* **28**, 17372-17380 (2012).

121. Coppage, R. *et al.* Determining peptide sequence effects that control the size, structure, and function of

nanoparticles. *ACS nano* **6**, 1625-1636 (2012).

122. Bhandari, R., Pacardo, D. B., Bedford, N. M., Naik, R. R. & Knecht, M. R. Structural control and catalytic reactivity of peptide-templated Pd and Pt nanomaterials for olefin hydrogenation. *The Journal of Physical Chemistry C* **117**, 18053-18062 (2013).

123. Sawoo, S., Srimani, D., Dutta, P., Lahiri, R. & Sarkar, A. Size controlled synthesis of Pd nanoparticles in water and their catalytic application in C–C coupling reactions. *Tetrahedron* **65**, 4367-4374 (2009).

124. McConnell, I., Li, G. & Brudvig, G. W. Energy conversion in natural and artificial photosynthesis. *Chemistry & Biology* **17**, 434-447 (2010).

125. Behrens, S. *et al.* Nanoscale particle arrays induced by highly ordered protein assemblies. *Advanced Materials* **14**, 1621-1625 (2002).

126. Kim, Y.-O. *et al.* A tyrosine-rich peptide induced flower-like palladium nanostructure and its catalytic activity. *RSC Advances* **5**, 78026-78029 (2015).

127. Selvakannan, P. *et al.* Synthesis of aqueous Au core-Ag shell nanoparticles using tyrosine as a pH-dependent reducing agent and assembling phase-transferred silver nanoparticles at the air-water interface. *Langmuir* **20**, 7825-7836 (2004).

128. Teranishi, T. & Miyake, M. Size control of palladium nanoparticles and their crystal structures. *Chemistry of Materials* **10**, 594-600 (1998).

129. Chen, A. K. & Woody, R. W. Theoretical study of the optical rotatory properties of poly-L-tyrosine. *Journal of the American Chemical Society* **93**, 29-37 (1971).

130. Woody, R. W. Aromatic side-chain contributions to the far ultraviolet circular dichroism of peptides and proteins. *Biopolymers* **17**, 1451-1467 (1978).

131. Jackson, M. & Mantsch, H. H. The use and misuse of FTIR spectroscopy in the determination of protein structure. *Critical Reviews in Biochemistry and Molecular Biology* **30**, 95-120 (1995).

132. Juszczyk, P., Kołodziejczyk, A. S. & Grzonka, Z. FTIR

spectroscopic studies on aggregation process of the β-amyloid 11−28 fragment and its variants. *Journal of Peptide Science* **15**, 23-29 (2009).

133. Barth, A. The infrared absorption of amino acid side chains. *Progress in Biophysics and Molecular biology* **74**, 141-173 (2000).

134. Nandurkar, N. S. & Bhanage, B. M. Palladium bis (2, 2, 6, 6-tetramethyl-3, 5-heptanedionate) catalyzed Suzuki, Heck, Sonogashira, and cyanation reactions. *Tetrahedron* **64**, 3655-3660 (2008).

135. Cheng, J. *et al.* A copper-and amine-free Sonogashira reaction employing aminophosphines as ligands. *The Journal of organic chemistry* **69**, 5428-5432 (2004).

136. Narayanan, R. & El-Sayed, M. A. Effect of catalysis on the stability of metallic nanoparticles: Suzuki reaction catalyzed by PVP-palladium nanoparticles. *Journal of the American Chemical Society* **125**, 8340-8347 (2003).

137. Breslow, R. Hydrophobic effects on simple organic reactions in water. *Accounts of Chemical Research* **24**,

159-164 (1991).

138. Putta, C. B. & Ghosh, S. Palladium nanoparticles on amphiphilic carbon spheres: A green catalyst for Suzuki–Miyaura reaction. *Advanced Synthesis & Catalysis* **353**, 1889-1896 (2011).

139. Kamal, A. *et al.* Water mediated Heck and Ullmann couplings by supported palladium nanoparticles: importance of surface polarity of the carbon spheres. *Green Chemistry* **14**, 2513-2522 (2012).

140. Chesterfield, R. J. *et al.* Variable temperature film and contact resistance measurements on operating n-channel organic thin film transistors. *Journal of Applied Physics* **95**, 6396-6405 (2004).

141. Schmidt, R. d. *et al.* High-performance air-stable n-channel organic thin film transistors based on halogenated perylene bisimide semiconductors. *Journal of the American Chemical Society* **131**, 6215-6228 (2009).

142. Peumans, P., Uchida, S. & Forrest, S. R. Efficient bulk

heterojunction photovoltaic cells using small-molecular-weight organic thin films. *Nature* **425**, 158-162 (2003).

143. Li, C. & Wonneberger, H. Perylene imides for organic photovoltaics: yesterday, today, and tomorrow. *Advanced Materials* **24**, 613-636 (2012).

144. Chen, S. *et al.* 1D nanofiber composites of perylene diimides for visible-light-driven hydrogen evolution from water. *RSC Advances* **4**, 48486-48491 (2014).

145. Langhals, H. Cyclic carboxylic imide structures as structure elements of high stability. Novel developments in perylene dye chemistry. *Heterocycles* **1**, 477-500 (1995).

146. Jones, B. A., Facchetti, A., Wasielewski, M. R. & Marks, T. J. Tuning orbital energetics in arylene diimide semiconductors. Materials design for ambient stability of n-type charge transport. *Journal of the American Chemical Society* **129**, 15259-15278 (2007).

147. Tang, M. L., Oh, J. H., Reichardt, A. D. & Bao, Z. Chlorination: a general route toward electron transport in

organic semiconductors. *Journal of the American Chemical Society* **131**, 3733-3740 (2009).

148. Jung, B. J., Tremblay, N. J., Yeh, M.-L. & Katz, H. E. Molecular design and synthetic approaches to electron-transporting organic transistor semiconductors. *Chemistry of Materials* **23**, 568-582 (2010).

149. Jiang, W. *et al.* Bay-linked perylene bisimides as promising non-fullerene acceptors for organic solar cells. *Chemical Communications* **50**, 1024-1026 (2014).

150. Wu¨rthner, F. *et al.* Perylene bisimide dye assemblies as archetype functional supramolecular materials. *Chemical Reviews* **116**, 962-1052 (2015).

151. Graser, F. & Hädicke, E. Kristallstruktur und Farbe bei Perylen-3, 4: 9, 10-bis (dicarboximid)-Pigmenten. *Liebigs Annalen der Chemie* **1980**, 1994-2011 (1980).

152. Graser, F. & Hädike, E. Kristallstruktur und Farbe bei Perylen-3, 4: 9, 10-bis (dicarboximid)-Pigmenten, 2. *Liebigs Annalen der Chemie* **1984**, 483-494 (1984).

153. Hädicke, E. & Graser, F. Structures of eleven perylene-3,

4: 9, 10-bis (dicarboximide) pigments. *Acta Crystallographica Section C: Crystal Structure Communications* **42**, 189-195 (1986).

154. Hädicke, E. & Graser, F. Structures of three perylene-3, 4, 9, 10-bis (dicarboximide) pigments. *Acta Crystallographica Section C: Crystal Structure Communications* **42**, 195-198 (1986).

155. Klebe, G., Graser, F., Hädicke, E. & Berndt, J. Crystallochromy as a solid-state effect: correlation of molecular conformation, crystal packing and colour in perylene-3, 4: 9, 10-bis (dicarboximide) pigments. *Acta Crystallographica Section B: Structural Science* **45**, 69-77 (1989).

156. Osswald, P. & Würthner, F. Effects of bay substituents on the racemization barriers of perylene bisimides: resolution of atropo-enantiomers. *Journal of the American Chemical Society* **129**, 14319-14326 (2007).

157. Gsänger, M. *et al.* A crystal-engineered hydrogen-bonded octachloroperylene diimide with a twisted core:

An n-channel organic semiconductor. *Angewandte Chemie International Edition* **49**, 740-743 (2010).

158. Rybtchinski, B., Sinks, L. E. & Wasielewski, M. R. Photoinduced electron transfer in self-assembled dimers of 3-fold symmetric donor-acceptor molecules based on perylene-3, 4: 9, 10-bis (dicarboximide). *The Journal of Physical Chemistry A* **108**, 7497-7505 (2004).

159. Osasa, T., Yamamoto, S., Iwasaki, Y. & Matsumura, M. Photocarrier generation in organic thin-film solar cells with an organic heterojunction. *Solar Energy Materials and Solar Cells* **90**, 1519-1526 (2006).

160. Lefler, K. M., Co, D. T. & Wasielewski, M. R. Self-assembly-induced ultrafast photodriven charge separation in perylene-3, 4-dicarboximide-based hydrogen-bonded foldamers. *The journal of physical chemistry letters* **3**, 3798-3805 (2012).

161. Draper, E. R. *et al.* Self-sorted photoconductive xerogels. *Chemical Science* **7**, 6499-6505 (2016).

162. Che, Y. *et al.* Ultrathin n-type organic nanoribbons with

high photoconductivity and application in optoelectronic vapor sensing of explosives. *Journal of the American Chemical Society* **132**, 5743-5750 (2010).

163. Walsh, J. J. *et al.* Controlling visible light driven photoconductivity in self-assembled perylene bisimide structures. *The Journal of Physical Chemistry C* **120**, 18479-18486 (2016).

164. Park, S., Lim, B. T., Kim, B., Son, H. J. & Chung, D. S. High mobility polymer based on a π-extended benzodithiophene and its application for fast switching transistor and high gain photoconductor. *Scientific reports* **4** (2014).

165. Decker, C. The use of UV irradiation in polymerization. *Polymer International* **45**, 133-141 (1998).

166. Sapagovas, V., Gaidelis, V., Kovalevskij, V. & Undzenas, A. 3, 4, 9, 10-Perylenetetracarboxylic acid derivatives and their photophysical properties. *Dyes and pigments* **71**, 178-187 (2006).

167. Farooqi, M. J., Penick, M. A., Burch, J., Negrete, G. R.

& Brancaleon, L. Characterization of novel perylene diimides containing aromatic amino acid side chains. *Spectrochimica Acta Part A: Molecular and Biomolecular Spectroscopy* **153**, 124-131 (2016).

168. Bystranowska, D., Siejda, B., Ożyhar, A. & Kochman, M. The dityrosine cross-link as an intrinsic donor for assembling FRET pairs in the study of protein structure. *Biophysical Chemistry* **170**, 1-8 (2012).

169. Bai, S. *et al.* Differential self-assembly and tunable emission of aromatic peptide bola-amphiphiles containing perylene bisimide in polar solvents including water. *Langmuir* **30**, 7576-7584 (2014).

170. Jacob, J. S. *et al.* Human phagocytes employ the myeloperoxidase-hydrogen peroxide system to synthesize dityrosine, trityrosine, pulcherosine, and isodityrosine by a tyrosyl radical-dependent pathway. *Journal of Biological Chemistry* **271**, 19950-19956 (1996).

171. Lee, D.-I., Hwang, S., Choi, J. Y., Ahn, I.-S. & Lee, C.-H.

A convenient preparation of dityrosine via Mn (III)-mediated oxidation of tyrosine. *Process Biochemistry* **43**, 999-1003 (2008).

172. Struijk, C. W. *et al.* Liquid crystalline perylene diimides: architecture and charge carrier mobilities. *Journal of the American Chemical Society* **122**, 11057-11066 (2000).

173. Lindner, S. M., Kaufmann, N. & Thelakkat, M. Nanostructured semiconductor block copolymers: π–π Stacking, optical and electrochemical properties. *Organic Electronics* **8**, 69-75 (2007).

174. Würthner, F., Thalacker, C., Diele, S. & Tschierske, C. Fluorescent J-type aggregates and thermotropic columnar mesophases of perylene bisimide dyes. *Chemistry–A European Journal* **7**, 2245-2253 (2001).

175. Rapaport, H., Kjaer, K., Jensen, T. R., Leiserowitz, L. & Tirrell, D. A. Two-dimensional order in β-sheet peptide monolayers. *Journal of the American Chemical Society* **122**, 12523-12529 (2000).

176. Payamyar, P. *et al.* Synthesis of a covalent monolayer

sheet by photochemical anthracene dimerization at the air/water interface and its mechanical characterization by AFM indentation. *Advanced Materials* **26**, 2052-2058 (2014).

177. Murray, D. J. *et al.* Large area synthesis of a nanoporous two-dimensional polymer at the air/water interface. *Journal of the American Chemical Society* **137**, 3450-3453 (2015).

178. Payamyar, P. *et al.* Approaching two-dimensional copolymers: Photoirradiation of anthracene-and diaza-anthracene-bearing monomers in Langmuir monolayers. *Macromolecular Rapid Communications* **36**, 151-158 (2015).

179. Soci, C. *et al.* ZnO nanowire UV photodetectors with high internal gain. *Nano Letters* **7**, 1003-1009 (2007).

180. Roy, S., Maiti, D. K., Panigrahi, S., Basak, D. & Banerjee, A. A new hydrogel from an amino acid-based perylene bisimide and its semiconducting, photo-switching behaviour. *RSC Advances* **2**, 11053-11060

(2012).

181. Draper, E. R. *et al.* Air-stable photoconductive films formed from perylene bisimide gelators. *Journal of Materials Chemistry C* **2**, 5570-5575 (2014).

182. Yamada, Y., Nakamura, T., Yasui, S., Funakubo, H. & Kanemitsu, Y. Measurement of transient photoabsorption and photocurrent of BiFeO 3 thin films: Evidence for long-lived trapped photocarriers. *Physical Review B* **89**, 035133 (2014).

183. Boobalan, G., Imran, P., Manoharan, C. & Nagarajan, S. Fabrication of highly fluorescent perylene bisimide nanofibers through interfacial self-assembly. *Journal of Colloid and Interface Science* **393**, 377-383 (2013).

184. Van der Boom, T. *et al.* Charge transport in photofunctional nanoparticles self-assembled from zinc 5, 10, 15, 20-tetrakis (perylenediimide) porphyrin building blocks. *Journal of the American Chemical Society* **124**, 9582-9590 (2002).

185. Marcon, R. O. & Brochsztain, S. Aggregation of 3, 4, 9,

10-perylenediimide radical anions and dianions generated by reduction with dithionite in aqueous solutions. *The Journal of Physical Chemistry A* **113**, 1747-1752 (2009).

186. Takada, T. *et al.* Photocurrent generation enhanced by charge delocalization over stacked perylenediimide chromophores assembled within DNA. *Journal of the American Chemical Society* **136**, 6814-6817 (2014).

187. Supur, M. & Fukuzumi, S. Photodriven electron transport within the columnar perylenediimide nanostructures self-assembled with sulfonated porphyrins in water. *The Journal of Physical Chemistry C* **116**, 23274-23282 (2012).

188. Ghosh, S., Li, X. Q., Stepanenko, V. & Würthner, F. Control of H-and J-type π stacking by peripheral alkyl chains and self-sorting phenomena in perylene bisimide homo-and heteroaggregates. *Chemistry-A European Journal* **14**, 11343-11357 (2008).

요 약 (국문 초록)

자연계에서 단백질과 펩타이드는 20 가지 종류의 아미노산의 공유결합 그리고 비공유결합에 의해 체계적으로 자기조립되어 기능을 나타낸다. 다양한 아미노산 중에서 타이로신은 단백질의 접힘과 전자 전달을 하는 등의 독특한 성질을 갖는다. 최근에 타이로신의 이러한 성질을 이용, 기능성 재료를 만들고자하는 노력들이 행해지고 있다.

제 1장에서는 체계적으로 설계한 펩타이드(Tyr-Tyr-Ala-His-Ala-Tyr-Tyr, YYAHAYY) 를 주형으로 이용하여, 팔라듐 나노구조체를 합성하고, 촉매적 성질에 대해서 규명하였다. CD와 FT-IR 분석 결과를 통해서, 펩타이드가 팔라듐 나노입자의 크기와 모양을 조절하여, 꽃 모양의 구조체를 만들어 내는 데에 관여한다는 것이 확인되었다. 합성된 꽃 모양의 팔라듐 나노입자 (Pd NPs)는 YYAHAYY의 양친매성 때문에 물에서 잘 분산됨을 관찰할 수 있었다. 또한 꽃 모양의 Pd NPs를 탄소-탄소 짝지음 반응 중에 하나인 소노가시라 반응의 촉

매로써 응용을 해본 결과 물을 용매로 하면서 온화한 조건에서 공촉매를 사용하지 않으면서 효율적인 촉매 활성을 나타내는 것으로 확인했다. 이를 통해 체계적으로 설계된 펩타이드를 주형이 팔라듐 나노입자의 크기, 모양, 표면들을 개질할 수 있으며, 촉매적 성질까지 조절할 수 있음을 확인하였다.

제 2장에서는 다이타이로신 가교 결합을 이용하여 퍼릴렌 다이이미드를 물/공기 계면에서 이차원 자기조립시켰으며, 이 물질이 광전류 성질이 있음을 규명하였다. 즉, 퍼릴렌 다이이미드는 pH 10 수용액에 자외선 (254 nm)를 조사함으로써 별도의 주형을 사용하지 않고 이차원으로 다이타이로신 가교결합에 의해 자기조립이 됨을 확인하였다. 이는 가교된 분자들의 양친매성에 의한 것으로 생각되며, 자외선 조사 시간에 따라 diTyr 가교가 증가하면서, 필름의 두께도 증가하여 조절이 가능함을 밝혔다. 또한, 가교가 일어남과 동시에 PDI 간의 파이-파이 상호작용으로 인하여 필름이 쌓여 반결정성을 나타냈으며, PDI의 빛 흡수 능력으로 인하여 광활성을 보임을 확인하였다.

주요어 : 자기조립, 펩타이드 자기조립, 생체유래 접근, 펩타이드 주형, 타이로신, 다이타이로신, 생광물화, 팔라듐, 촉매, 교차 짝지음, 구리-없는 소노가시라 반응, 유기 반도체, 퍼릴렌 다이이미드, 광전류

학 번 : 2011-21021